

**MODELLING OF MOIRÉ SUPERLATTICES OF
HETEROBILAYER STRUCTURES USING
CONTINUUM QUANTUM MONTE CARLO
METHODS**

**A Thesis Submitted to
the Graduate School of Engineering and Sciences of
İzmir Institute of Technology
in Partial Fulfillment of the Requirements for the Degree of**

DOCTOR OF PHILOSOPHY

in Materials Science and Engineering

**by
Mustafa Neşet ÇINAR**

**December 2024
İZMİR**

We approve the thesis of **Mustafa Neşet ÇINAR**

Examining Committee Members:

Prof. Dr. Alev Devrim GÜÇLÜ

Department of Physics, İzmir Institute of Technology

Prof. Dr. Ramazan Tuğrul SENER

Department of Physics, İzmir University of Economics

Prof. Dr. Gürsoy Bozkurt AKGÜÇ

Department of Physics, İzmir University of Economics

Asst. Prof. Dr. Mahmut Barış OKATAN

Department of Materials Science and Engineering, İzmir Institute of Technology

Asst. Prof. Dr. Evren ATAMAN

Department of Physics, İzmir Institute of Technology

13 December 2024

Professor Dr. Alev Devrim GÜÇLÜ

Department of Physics
İzmir Institute of Technology

Assoc. Prof. Dr. Umut ADEM

Department of
Materials Science and Engineering
İzmir Institute of Technology

Prof. Dr. Yaşar AKDOĞAN

Head of the Department of
Materials Science and Engineering

Prof. Dr. Mehtap EANES

Dean of the Graduate School of
Engineering and Sciences

ACKNOWLEDGMENTS

I would like to express my deepest gratitude to my thesis advisor, Alev Devrim GÜÇLÜ, for giving me the opportunity to be a part of his research group. His invaluable guidance, patience, and feedback have been instrumental to my growth in this field. I learned a great deal from him despite the challenges of such a limited timeframe for my thesis.

I would like to thank Pawel Potasz for his insightful suggestions and discussions on Moiré heterostructures, which offered valuable perspectives for this study. I am also grateful to my co-advisor, Umut ADEM, and professors Özgür ÇAKIR and Mahmut Barış OKATAN for their valuable contributions to my monitoring exams through fruitful discussions and insights. My sincere thanks go to the defense jury members, Ramazan Tuğrul SENER, Gürsoy Bozkurt AKGÜÇ and Evren ATAMAN, for their time, insightful questions, and inspiring suggestions for future work.

I would also like to thank the members of our research group Gökhan ÖZTARHAN, Erdoğan Bulut KUL and Emre OKÇU, who are also my office mates, for engaging discussions on various topics. I am especially grateful to Gökhan for the valuable discussions on the CHAMP code and continuum Monte Carlo simulations.

I would be remiss not to acknowledge the friends and colleagues whose conversations have provided moments of camaraderie and moral support throughout my PhD journey. Special thanks go to my best friend, İsmail ULUS, whose encouragement and steadfast support have helped me stay motivated and uplifted throughout this journey.

Lastly, I could not have undertaken this journey without my mother and father. Their unconditional love, unwavering support, and never-ending belief in me have been a constant source of strength, enabling me to overcome numerous challenges throughout my life.

This research is supported by TÜBİTAK (122F345). The numerical calculations reported in this paper were partially performed at TÜBİTAK ULAKBİM, High Performance and Grid Computing Center (TRUBA resources).

ABSTRACT

MODELLING OF MOIRÉ SUPERLATTICES OF HETEROBILAYER STRUCTURES USING CONTINUUM QUANTUM MONTE CARLO METHODS

Moiré heterostructures of transition metal dichalcogenides (TMD) show exotic physical phenomena such as insulating phase at half-filling, Wigner crystallization and itinerant (Stoner) ferromagnetism. Itinerant (Stoner) ferromagnetism can be explained through favored ferromagnetic configurations due to exchange interactions between the electrons occupying similar energy levels. The charge carrier dynamics in such materials is determined by a potential called moiré potential that forms a triangular lattice. Moiré potential can be defined as a sum of Gaussians for finite structures. Tight-Binding (TB) model is the simplest approximation used to understand electronic systems with non-interacting particles by using localized orbitals in real space. Hubbard model is a many-body extension of TB model by incorporation of Coulomb repulsion between electrons. Mean-field approximation of Hubbard model (Mean-Field Hubbard, MFH) can be used to solve for ground state self-consistently. Variational Monte Carlo (VMC) and Diffusion Monte Carlo (DMC) are continuum Monte Carlo methods that are used for calculating ground state energies and spin-dependent densities of correlated electrons accurately in both real and artificial lattices. Trial wave functions are initial wave functions for VMC and DMC calculations given in Slater-Jastrow form. In this study, in order to investigate magnetic phases of finite-size moiré heterostructures, a finite moiré potential for MoSe₂/WS₂ heterobilayers is defined, and DMC calculations were performed by using VMC-optimized TB and ground-state MFH orbitals. Our findings show the presence of ferromagnetic ground state at 3/2 filling where van Hove singularity occurs. For larger potential amplitude, Wigner crystal states around 1/3 filling were observed as excited states.

ÖZET

HETEROBİLAYER YAPILARIN MOIRÉ SÜPER KAFESLERİNİN SÜREKLİ KUANTUM MONTE CARLO TEKNİKLERİ KULLANILARAK MODELLENMESİ

Geçiş metali dikalkojenitlerinin Moiré heteroyapıları, yarı dolumda yalıtkan hal, Wigner kristalizasyonu ve gezgin (Stoner) ferromanyetizması gibi egzotik fiziksel olgular göstermektedir. Gezgin (Stoner) ferromanyetizması, benzer enerji seviyelerindeki elektronlar arasındaki değişim etkileşimlerine bağlı olarak tercih edilen ferromanyetik konfigürasyonlar ile açıklanabilmektedir. Bu tür malzemelerde yük taşıma dinamikleri üçgen örgü oluşturan ve moiré potansiyeli adı verilen bir potansiyel tarafından belirlenmektedir. Moiré potansiyel, sonlu yapılar için Gausyenlerin bir toplamı olarak tanımlanabilmektedir. Sıkı Bağlam (TB) modeli, gerçek uzayda lokalize orbitaller kullanılarak etkileşmeyen parçacıklara sahip elektronik sistemleri anlamak için kullanılan en basit yaklaşımdır. Hubbard modeli, elektronlar arasındaki Coulomb itme kuvvetinin dahil edilmesiyle sıkı bağlam modelinin çok cisimli bir uzantısıdır. Hubbard modelinin ortalama alan yaklaşımı (ortalama alan Hubbard, MFH) temel hali öz-uyumlu bir şekilde çözmek için kullanılabilir. Varyasyonel Monte Carlo (VMC) ve Difüzyon Monte Carlo (DMC); korele elektronların temel hal enerjilerini ve spine bağlı yoğunluklarını hem gerçek hem de yapay örgülerde doğru bir şekilde elde etmek için kullanılmaktadır. Deneme dalga fonksiyonları, VMC ve DMC hesapları için Slater-Jastrow formunda verilen başlangıç dalga fonksiyonlarıdır. Bu çalışmada, sonlu büyüklükteki moiré heteroyapıların manyetik fazlarını araştırmak üzere $\text{MoSe}_2/\text{WS}_2$ hetero-çift katmanları için sonlu moiré potansiyeli tanımlanarak VMC ile optimize edilmiş TB ve temel hal MFH orbitalleri kullanılarak DMC hesapları gerçekleştirilmiştir. Bulgularımız, van Hove tekilliğinin bulunduğu 3/2 dolumda ferromanyetik temel halin varlığını göstermektedir. Daha büyük potansiyel için 1/3 dolum civarında uyarılmış hal olarak Wigner kristali gözlenmektedir.

To my mother and father.

TABLE OF CONTENTS

LIST OF FIGURES	viii
LIST OF TABLES	xii
LIST OF ALGORITHMS	xiii
LIST OF SYMBOLS	xiv
LIST OF ABBREVIATIONS	xv
CHAPTER 1. INTRODUCTION	1
1.1. Moiré Superlattices	1
1.2. Moiré Potential	3
1.3. Itinerant (Stoner) Ferromagnetism	6
1.4. Wigner crystallization	9
CHAPTER 2. METHODS	11
2.1. Moiré Potential for Finite Lattices	11
2.2. Tight-Binding Model	15
2.3. Mean-Field Hubbard Model	21
2.4. Variational Monte Carlo Method	27
2.5. Diffusion Monte Carlo Method	29
CHAPTER 3. RESULTS	32
3.1. 16-site Rhombohedral Lattice	32
3.2. 19-site Radial Lattice With Guiding Potential	40
3.3. Wigner Crystals	43
CHAPTER 4. CONCLUSION	47

LIST OF FIGURES

<u>Figure</u>	<u>Page</u>
Figure 1.1. (a) Type-I and (b) type-II band alignments are shown. The highest valence band and the lowest conduction band are depicted by green and red lines respectively. The highest valence and the lowest conduction band are located in the same layer in type-I band alignment, however, they are located in different layers in type-II band alignment.	3
Figure 1.2. (a) Isolated valence band (so-called moiré band), (b) type-II band alignment, (c) moiré potential in a unit cell of triangular lattice, and (d) periodic moiré potential in WSe ₂ /WS ₂ heterobilayers. (Source: ref 22)	4
Figure 1.3. Visualization of Wigner crystals on WSe ₂ /WS ₂ heterobilayers are shown. (Source: ref 11)	5
Figure 1.4. (a) Moiré conduction bands and (b) interlayer distance of MoSe ₂ /WS ₂ heterobilayers. Letters M and X correspond to the transition metal elements (Mo, W) and the chalcogenide elements (Se, S) respectively. Therefore, sites denoted by MM, XM and MX show interlayer stacking of Mo-W, Se-S, S-Se pairs respectively. (Source: ref 32)	5
Figure 1.5. (a) Total spin with respect to the filling factor in WS ₂ /WSe ₂ heterobilayers (half-filling is defined as $\nu = 0.5$ for this figure). (Source: ref 33) (b) Temperature multiplied by susceptibility $T\chi$ with respect to the filling factor ν for three different temperature values. Paramagnetic for $\nu < 1$, ferromagnetic for $1 < \nu < 3/2$ and antiferromagnetic for $\nu > 3/2$. (Source: ref 32)	7
Figure 2.1. (a), (b) and (c) show Gaussian-like functions that are used in the sum potential (Fig. 2.2) at minima, maxima and midpoints respectively. (a) and (b) are ordinary Gaussians that are slightly curved, i.e. $s \approx 1$, whereas (c) becomes more flat around its center with negative stiffness, differing from Gaussians.	13
Figure 2.2. (a) Bulk Moiré Potential in a 7x7 triangular lattice given by eq. 1.1 with $V_m = 6.3$ meV and $\psi = 0^\circ$ for MoSe ₂ /WS ₂ . ³² (b) Finite moiré	

	potential given by eq. 2.2 the fitted to the bulk Moiré potential inside. Black, green and red squares correspond to wells, hills and midpoint sublattices. (c) Absolute difference between fitted potential and moiré potential is shown.	13
Figure 2.3.	Top-view (a) and side-view (b) of the resulting finite moiré potential is shown in eV. Bias V_b is shifted such that the maxima goes to zero outside the system.	14
Figure 2.4.	(a) Finite two-level system in which two atoms are coupled to each other with a hopping amplitude t . (b) Infinite diatomic chain with consists of two atoms per unit cell with nearest-neighbor coupling. ...	16
Figure 2.5.	(a) Energy band diagram and (b) density of states of diatomic chain shown in Fig. 2.4.	17
Figure 2.6.	(a) Triangular lattice site in the center and its neighbors translated by $n\vec{a}_1 + m\vec{a}_2$ with $n, m \in 0, \pm 1$, and (b) the reciprocal lattice site in the center and its neighbors translated by $n\vec{b}_1 + m\vec{b}_2$ with $n, m \in 0, \pm 1$ are shown. The first Brillouin zone is shown by black hexagon, and high-symmetry points are annotated by black symbols. (c) Energy band diagram and (d) density of states are also shown.	18
Figure 3.1.	4x4 triangular lattice used used in TB and MFH calculations are shown. Lattice points are shown by red circles while the couplings between the nearest neighbor sites are shown by black lines.	32
Figure 3.2.	Spin densities, charge densities, energy spectrum and DOS of MFH ground state ($S_z = 0$) of 4x4 rhombohedral lattice is shown. Red and blue colors correspond to down and up orbitals in energy and DOS figures. The interaction strength is $\kappa U/t = 2$, where κ is relative dielectric constant.	33
Figure 3.3.	For 4x4 rhombohedral lattice, ground state ($S_z = 1$) spin- \uparrow - spin- \downarrow densities (column 1-2), spin densities (column 3) and charge densities (column 4) for (a) VMC with TB trial w.f., (b) VMC with MFH trial w.f., (c) DMC with VMC-optimized TB trial w.f., (d) DMC with VMC-optimized MFH trial w.f. are shown. Density plots for DMC calculations in (c) and (d) are extrapolated by using equation 2.78. ...	37

- Figure 3.4. For 4x4 rhombohedral lattice, ground state extrapolated spin- \uparrow - spin- \downarrow densities (column 1-2), extrapolated spin densities (column 3) and extrapolated charge densities (column 4) for (a) $\nu = 1/2$, (b) $\nu = 1$ and (c) $\nu = 3/2$ 38
- Figure 3.5. For (a) 4x4 rhombohedral unit cell sites are shown by black dots, unit cells translated by \vec{a}_1 and \vec{a}_2 vectors are shown by blue and red dots. (b) Band structure obtained by using first nearest-neighbor TB model with hopping parameter $t = 1$ for aforementioned unit cell. (c) DOS obtained by equation 2.26 is shown. Blue lines and red lines correspond to DOS of periodic and finite lattices respectively. Discrete energy levels of finite system are depicted by horizontal dashed lines. Left and right y-axes correspond to energy E and filling factor ν respectively. Van Hove singularity occurs at $E = 2t$ or $\nu = 3/2$ 39
- Figure 3.6. (a) TB spectrum for 4x4 rhombohedral lattice (red circles). Blue dotted lines correspond to the expected S_z values for expected spin values due to degeneracies in TB spectrum. Magenta squares correspond to the ground state S_z values obtained from DMC calculations. Some of the calculations resulted in multiple S_z values within an error bar around minimum energy. Lower S_z values are shown by gray squares. (b) Orbital occupation of singly occupied orbitals for 24 electrons. ... 41
- Figure 3.7. 19-site radial lattice used used in tight-binding and mean-field Hubbard calculations are shown. Lattice points are shown by red circles while the couplings between the nearest neighbor sites are shown by black lines. 42
- Figure 3.8. (a) Moiré potential, (b) Moiré potential with guiding potential and (c) guiding potential for radial 19-site lattice in eV. Black, red and green squares correspond to potential wells, hills and midpoints respectively. Guiding gaussian amplitude $V_g = -28V_m = -176.4$ meV, stiffness $s_g = 0.8$ and width ρ_g is at the order of the size of the lattice. 42
- Figure 3.9. Ground state spin and charge densities obtained by DMC calculations by using VMC-optimized TB trial wave functions for (a) 10 electrons ($\nu = 10/19 = 0.5263$, $S_z = 1$), (b) 19 electrons ($\nu = 1$, $S_z = 1/2$), (c)

30 electrons ($\nu = 30/19 = 1.579$, $S_z = 3$).....	43
Figure 3.10. (a) TB spectrum for 19-site radial lattice (red circles). Blue dotted lines correspond to the expected S_z values for expected spin values due to degeneracies in TB spectrum. Magenta squares correspond to the ground state S_z values obtained from DMC calculations. Some of the calculations resulted in multiple S_z values within an error bar around minimum energy. Lower S_z values are shown by gray squares.	
(b) Orbital occupation of singly occupied orbitals for 30 electrons. ...	44
Figure 3.11. Extrapolated charge densities for (a) $S_z = 7/2$, (b) $S_z = 5/2$, (c) $S_z = 3/2$ and (d) $S_z = 1/2$	45
Figure 3.12. Extrapolated pair polarization $D_{\uparrow\uparrow} - D_{\uparrow\downarrow}$ (a) $S_z = 1/2$ and (b) $S_z = 3/2$. The fixed site is shown inside the red circle.	46
Figure 3.13. Extrapolated spin and charge densities for (a) $S_z = 1/2$, (b) $S_z = 3/2$, (c) $S_z = 5/2$ and (d) $S_z = 7/2$	46

LIST OF TABLES

<u>Table</u>	<u>Page</u>
Table 3.1. Acceptance rates, total energies, and RMS errors in total energies of VMC calculations performed by using TB and MFH trial wave functions.....	35
Table 3.2. Acceptance rates, ratios of correlation times to number of steps, total energies, RMS errors in total energies and population control errors of DMC calculations performed by using VMC-optimized TB trial wave functions for $\nu = 1$ in 4x4 rhombohedral lattice.....	35
Table 3.3. Acceptance rates, ratios of correlation times to number of steps, total energies, RMS errors in total energies and population control errors of DMC calculations performed by using VMC-optimized MFH trial wave functions for $\nu = 1$ in 4x4 rhombohedral lattice.....	36
Table 3.4. For 4x4 rhombohedral lattice, 8 e^- ($\nu = 1/2$) VMC acceptance, energies and RMS errors for each S_z . The lowest energy trial wavefunctions are shown.....	36
Table 3.5. For 4x4 rhombohedral lattice, 24 e^- ($\nu = 3/2$) VMC acceptance, energies and RMS errors for each S_z . The lowest energy trial wavefunctions are shown.....	38
Table 3.6. For 4x4 rhombohedral lattice, 8 e^- ($\nu = 1/2$) DMC acceptance, correlation time-number of steps ratio, energies, RMS errors and population control errors for each S_z . The lowest energy trial wavefunctions are shown.....	39
Table 3.7. For 4x4 rhombohedral lattice, 24 e^- ($\nu = 3/2$) DMC acceptance, correlation time-number of steps ratio, energies, RMS errors and population control errors for each S_z . The lowest energy trial wavefunctions are shown.....	40
Table 3.8. S_z , energy, RMS error in energy and population control error for 7 electrons in 19-site radial lattice with $V_m = 25$ meV.....	44

LIST OF ALGORITHMS

<u>Algorithm</u>	<u>Page</u>
Algorithm 2.1. Self-Consistent Mean-Field Hubbard algorithm	25
Algorithm 2.2. Adaptive mixing algorithm for self-consistent MFH calculations ..	26

LIST OF SYMBOLS

<u>Symbol</u>	<u>Definition</u>
\hbar	Reduced Planck's Constant
ϵ_0	Vacuum Dielectric Permittivity
ϵ	Dielectric Permittivity
κ	Relative Dielectric Permittivity
m_e	Electron Mass
m_{eff}	Effective Mass
m_r	Relative Effective Mass
a_B	Bohr Radius
a_B^*	Effective Bohr Radius
a_{WS}	Wigner-Seitz Radius
r_s	Wigner-Seitz Parameter
R_y	Rydberg Energy
R_y^*	Effective Rydberg Energy
n	Electron Density
ν	Filling Factor
V_m	Moiré Potential Amplitude
\hat{a}_j	Single Electron Annihilation Operator in Orbital j^{th}
\hat{a}_j^\dagger	Single Electron Creation Operator in Orbital j
\mathcal{E}_j	On-site Energy in Orbital j
t_{ij}	Hopping Parameter Between Orbitals i and j
\mathcal{D}	Density of States
$\hat{c}_{j\sigma}$	Many Electron Annihilation Operator in Orbital j and Spin σ
$\hat{c}_{j^\dagger\sigma}$	Many Electron Creation Operator in Orbital j and Spin σ
$\hat{n}_{j\sigma}$	Number Operator of Orbital j and Spin σ
U	On-Site Hubbard Energy
E_n	Energy Level of Orbital n
S_z	Spin in Z-Direction

LIST OF ABBREVIATIONS

<u>Abbreviation</u>	<u>Definition</u>
2DEG	Two Dimensional Electron Gas
CHAMP	Cornell - Holland Ab-initio Materials Package
DFT	Density Functional Theory
DMC	Diffuson Monte Carlo
DOS	Density of States
MFH	Mean-Field Hubbard
RMS	Root Mean Square
TB	Tight-Binding
TMD	Transition Metal - Dichalcogenide
VMC	Variational Monte Carlo

CHAPTER 1

INTRODUCTION

Low dimensional materials has been study of interest in physics and materials science for nearly over two decades since the first graphene flake is produced by Novoselov and Geim.¹ Graphene is a conductor with linear dispersion relation causing electrons to travel with higher speeds than the electrons in ordinary conductors such as copper that we use in our daily lives. Despite these interesting properties, graphene does not have a band gap. Thus, semiconductor industry has been focusing on finding alternative low dimensional materials with a reasonable band gap to build switching mechanisms for electric current. Accordingly, two dimensional Transition Metal - Dichalcogenide (TMD) materials are found to be viable alternatives to graphene as they are semiconductors.² Alternatively, nanostructured low dimensional materials such as graphene nanoribbons,³ graphene anti-dot lattices,⁴ bilayer graphene⁵ and TMD bilayers⁶ are shown to have considerable band gap for electronic applications.

Apart from band semiconductors, strong electronic correlations in materials can lead to tunable insulating phases controlled by bandwidth, filling and dimensionality of materials.^{7,8} Strong correlation effects in these materials can lead to Wigner crystallization.⁹⁻¹²

The materials with strong electron correlations are considered for novel device applications such as field effect transistors,¹³⁻¹⁵ tunable superconductors,^{15,16} neuromorphic memristor devices.¹⁷

In this study, we focus on magnetic phases and magnetic phase transitions due to strong correlation in moiré heterostructures based on TMD heterobilayers by using continuum Monte Carlo methods.

1.1. Moiré Superlattices

Monolayer flakes of two dimensional materials can be stacked on top of each other to create bilayer structures. These bilayer structures can be twisted, i.e. one of the layers

is rotated with respect to other by an angle called twist angle. The local variations in the interlayer bond lengths create moiré patterns. These patterns may occur in homobilayers such as twisted bilayer graphene, or heterobilayers composed of two different materials. These structures are called moiré superlattices.

Recent studies on twisted bilayer graphene show that the electronic bands of moiré superlattices (moiré bands) can be flattened by tuning the twist angle,¹⁸ allowing strongly correlated charge carriers¹⁹ lead to interesting phases such as Mott insulator states and unconventional superconductivity.^{16,20}

Other than graphene, bilayer structures of two dimensional Transition Metal - Dichalcogenide (TMD) materials can be used to form Moiré superlattices. Two dimensional TMD materials are compounds with two chalcogenide atoms for every transition metal atom with chemical formula MX_2 (M: transition metal, X: chalcogenide). Moiré superlattices can be formed in homobilayers or heterobilayers of TMD materials.

Unlike graphene, broken inversion symmetry and spin-orbit coupling in TMD structures causes coupling between spin and valley degrees of freedom (so-called spin-valley locking).²¹ Additionally, in heterobilayer TMDs, the band alignment between layers determine the preferred layer for carrier motion. In heterobilayer TMDs with type-I band alignment, the lowest conduction band and the highest valence band are located in the same material. For instance, $\text{MoSe}_2/\text{WS}_2$ has type-I band alignment with both the highest valence band and the lowest conduction band in MoSe_2 . On the other hand, in heterobilayer TMDs with type-II band alignment, conduction band and valence band are located in different materials. As an example, in WSe_2/WS_2 heterobilayers, the holes in the highest valence band exist on WSe_2 layer whereas the electrons in the lowest conduction band exist in WS_2 layer.^{6,10,22–26} Similarly, $\text{MoS}_2/\text{WSe}_2$ heterobilayer has type-II band alignment with conduction band in MoS_2 .^{6,27} Figure 1.1 shows type-I and type-II band alignments. Although these are the intrinsic band alignments for these materials, a recent study showed that the band alignment of $\text{MoSe}_2/\text{WS}_2$ can be changed by strong electric fields.²⁸

The reduced degrees of freedom due to broken symmetries in heterobilayer TMDs provide a framework for modeling by single-band Hubbard models.^{22,24,25,29–33} Although these models capture the essential physics underlying these structures, most of them ignore higher order perturbative terms such as long-range electron-electron interactions. Alternatively, continuum Monte Carlo methods such as Variational Monte Carlo and Diffusion

Monte Carlo methods can be used to determine ground state of Moiré superlattices without ignoring higher-order terms.

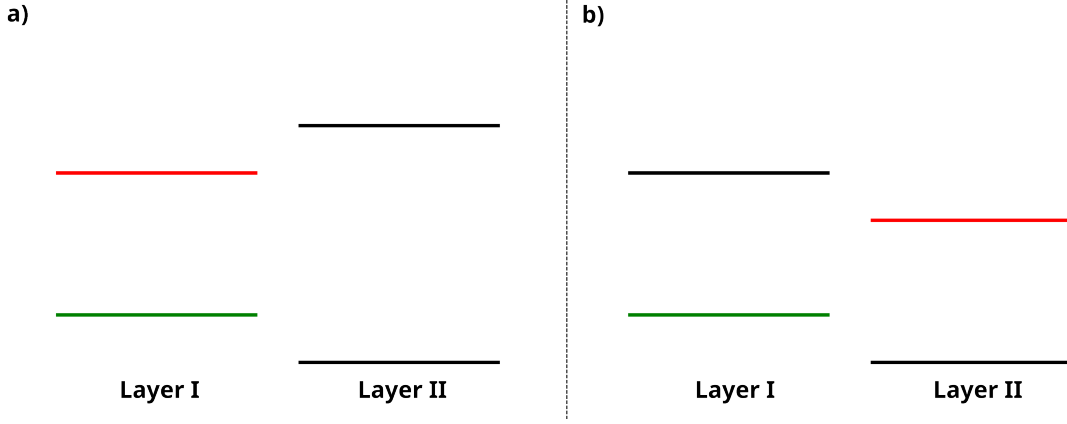


Figure 1.1. (a) Type-I and (b) type-II band alignments are shown. The highest valence band and the lowest conduction band are depicted by green and red lines respectively. The highest valence and the lowest conduction band are located in the same layer in type-I band alignment, however, they are located in different layers in type-II band alignment.

1.2. Moiré Potential

The periodic potential that the the charge carriers (i.e. electrons and holes) in a moiré heterobilayer feel due to interlayer bonds can be modeled by,^{22,34}

$$V(\vec{r}) \approx \sum_{i=1,3,5} V_m \cos(\vec{b}_i \cdot \vec{r} + \psi) \quad (1.1)$$

where the modulation potential V_m and phase ψ are the system dependent parameters and b_i are the reciprocal lattice vectors. Figure 1.2c-d shows a Moire potential the extrema of which form a triangular lattice. The parameters of the potential are $V_m = 6.6$ meV and $\psi = -94^\circ$. Due to the moiré potential, the charge dynamics are different from natural solids in which crystal potentials determine the carrier motion. Accordingly, the interaction energy and length scales differ significantly. In natural solids, the typical length scale is at the order of atomic distance is $\sim \text{\AA}$ and the energy scale is \sim eV, while in moiré superlattices the typical length scale is at the order of 10 nm with interaction energies at the

order of 10-100 meV.²⁴ For instance, For for WSe₂/WS₂ heterobilayers the bandwidth is around 11 meV²² that determines the energy scales of the moiré potential and the kinetic energies of electrons (see Fig. 1.2a,c-d). In twisted bilayer TMDs, the periodic length a_M is approximated by $a_0/\sqrt{\theta^2 + \delta^2}$ where a_0 is the lattice constant of the layer with larger lattice constant, θ is the twist angle and δ is the lattice mismatch which is typically about 4%.²⁴ For instance, untwisted WSe₂/WS₂ heterobilayers, a_M is given as 8.2 nm²⁴ which corresponds to $a_0 \approx 0.328$ nm for WSe₂.³⁵

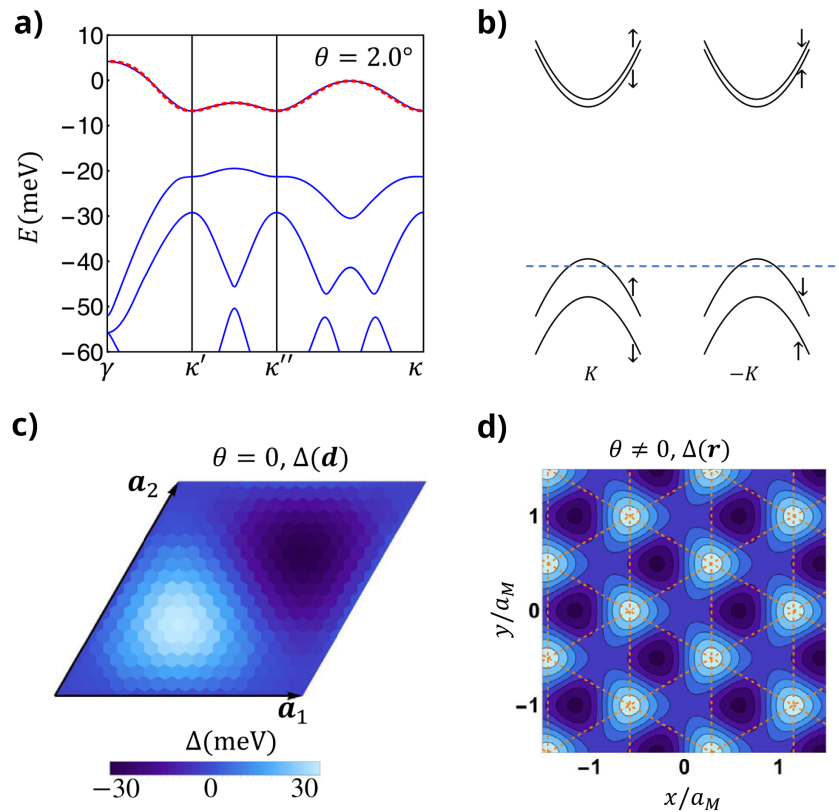


Figure 1.2. (a) Isolated valence band (so-called moiré band), (b) type-II band alignment, (c) moiré potential in a unit cell of triangular lattice, and (d) periodic moiré potential in WSe₂/WS₂ heterobilayers. (Source: ref 22)

Moiré potential is highly tunable due to its dependence on the interlayer coupling and the moiré period. The modulation potential V_m can be modified by gate controlled electric fields or external pressure,^{22,30,36} while the periodic length can be modified by the twist angle θ . Although both lattice hopping and Coulomb interaction depends on the Moiré potential, the latter also depends on the dielectric permittivity ϵ which can be tuned by varying the carrier density and the separation of the gates.³⁰ Hence, modifying V_m , θ

and ϵ allows one to probe correlated phases in twisted heterobilayer TMD structures.

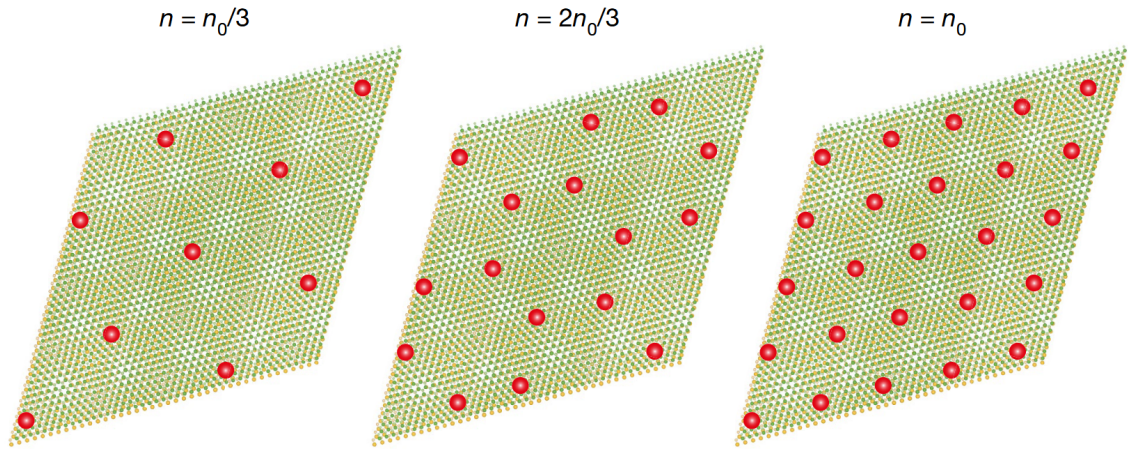


Figure 1.3. Visualization of Wigner crystals on WSe_2/WS_2 heterobilayers are shown.

(Source: ref 11)

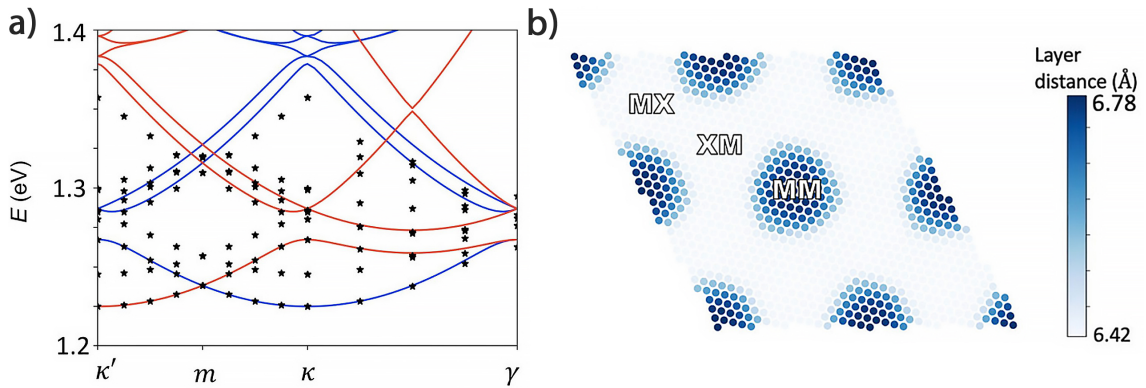


Figure 1.4. (a) Moiré conduction bands and (b) interlayer distance of $\text{MoSe}_2/\text{WS}_2$ heterobilayers. Letters M and X correspond to the transition metal elements (Mo, W) and the chalcogenide elements (Se, S) respectively. Therefore, sites denoted by MM, XM and MX show interlayer stacking of Mo-W, Se-S, S-Se pairs respectively. (Source: ref 32)

Recently, it has been shown that for the half-filled moiré valance band in WSe_2/WS_2 heterobilayers, the strong Coulomb interaction gives rise to an insulating phase.²² For twist angles larger than 3° , the long range spin exchange coupling becomes large enough to make spin-liquid state possible in half-filling.²² Van Hove singularity at filling $\nu = 3/2$ ($\nu = 1$: half filling) can give rise to four-sublattice antiferromagnetic phases which are related to interesting phenomena such as quantum anomalous Hall effect.²² The insulating phase

at half-filling has been verified experimentally in a later studies.^{11,25} It has also been argued that the insulating state at half-filling is a charge-transfer insulator instead of a Mott insulator.^{24,30} Additionally, Wigner crystal states are observed at $1/3$ and $2/3$ fillings,¹¹ which provides correlated phenomena such as frustrated magnetism³⁷ and quantum melting.³¹ The visualization of Wigner crystals at $\nu = 1/3$, $\nu = 2/3$ and $\nu = 1$ are shown in figure 1.3.

A recent experimental study investigated various correlated insulating phases such as Wigner crystals and charge density waves at fractional fillings for both holes and electrons in WSe_2/WS_2 heterobilayers by optical sensing via excitons.¹⁰ In addition to the verification of Wigner crystals at $1/3$ and $2/3$ hole filling, it has further been shown that Wigner crystal states are also present at $1/4$ hole filling and their conjugate electron filling factors $1-\nu$.¹⁰ Another experimental study on WSe_2/WS_2 by using microwave impedance microscopy agrees with the previous results on Wigner crystals at $1/3$ and $1/4$ fillings and their conjugate fillings for both electrons and holes.¹² Additional theoretical studies on WSe_2/WS_2 heterobilayers have showed tunable antiferromagnetic-ferromagnetic phase transitions^{29,38} and itinerant ferromagnetism at $3/2$ filling due to van Hove singularity are possible.³³ This behavior is observed in an experimental study on $\text{MoSe}_2/\text{WS}_2$ in which paramagnetic-ferromagnetic transition at $3/2$ filling can occur in.³² In $\text{MoSe}_2/\text{WS}_2$ heterobilayers, the band alignment is of type-I, thus the valence and conduction bands are symmetric due to the localization in the same material. The conduction bands obtained by DFT calculation are shown in Fig. 1.4a. The interlayer distance which determines the moiré potential is shown in Fig. 1.4b. Because the MM sites are more localized than that of WS_2/WSe_2 heterobilayers, the potential phase ψ is different, as well as the potential amplitude V_m which determines the band structure. Moiré potential parameters for WS_2/WSe_2 conduction bands are given by $V_m = 6.3$ meV and $\psi = 0^\circ$.

1.3. Itinerant (Stoner) Ferromagnetism

Van Hove singularities are the divergences that occur in the Density of States (DOS) of electronic systems. They are related to the narrow bandwidths, since DOS is simply the derivative of the band energies with respect to the energy.

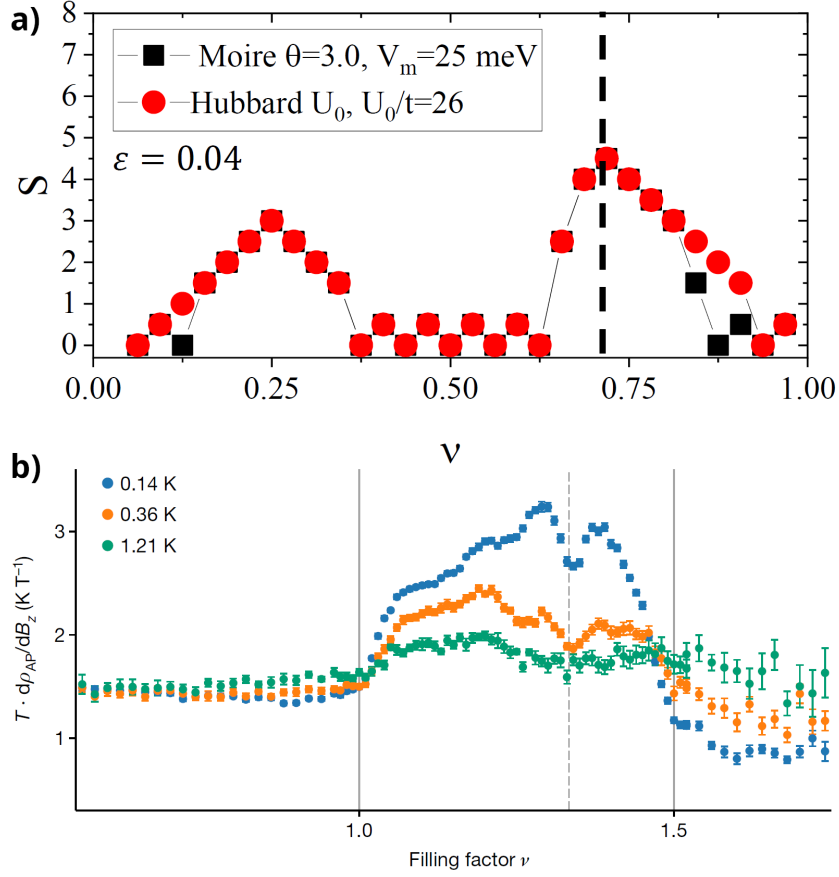


Figure 1.5. (a) Total spin with respect to the filling factor in WS_2/WSe_2 heterobilayers (half-filling is defined as $\nu = 0.5$ for this figure). (Source: ref 33) (b) Temperature multiplied by susceptibility $T\chi$ with respect to the filling factor ν for three different temperature values. Paramagnetic for $\nu < 1$, ferromagnetic for $1 < \nu < 3/2$ and antiferromagnetic for $\nu > 3/2$. (Source: ref 32)

Electron correlations in a material are enhanced when there is a van Hove singularity in density of states at the Fermi energy which is the highest occupied energy level. Around a van Hove singularity, there are many electrons which have similar energies. These electrons interact with each other more than the electrons with different energies. This behavior can be explained by using Fermi golden rule, which approximates the single-particle transition probability between two different energy levels under weak perturbation,³⁹

$$W_{i \rightarrow n} = \frac{2\pi}{\hbar} |V_{ni}|^2 \mathcal{D}(E_n) \quad (1.2)$$

where $W_{i \rightarrow n}$ is the transition probability per unit time (transition rate) between states $|i\rangle$

and $|n\rangle$ state, $V_{ni} = \langle n|\hat{V}|i\rangle$ is the expectation value of interaction potential between states $|i\rangle$ and $|n\rangle$, $\mathcal{D}(E)$ is DOS at energy E . Because the scattering rate (therefore the scattering probability) is proportional to DOS and a van Hove singularity at Fermi energy in DOS causes the most electrons to occupy similar energies, the interactions between these electrons become highly probable. Many-body electronic wavefunctions obey Pauli exclusion principle according to which multiple electrons having the same spin cannot occupy the same location. This causes the electrons with parallel spins stay apart, thereby reducing the Coulomb repulsion between them.³³ This type ferromagnetism is called itinerant or Stoner ferromagnetism, that is defined by Stoner's criterion,⁴⁰

$$I\mathcal{D}(E_F) > 1 \quad (1.3)$$

where I is the exchange coupling that corresponds to the energy gain per unit cell due to the parallel alignment of spins³³ and $\mathcal{D}(E_F)$ is the density of states at Fermi energy E_F . Theoretically, itinerant ferromagnetism is expected at $\nu = 3/2$ filling for triangular lattices where van Hove singularity occurs.^{32,41} Such ferromagnetism is shown for $\nu = 3/2$ ($\nu = 3/4$ in the figure, since half-filling is defined as $\nu = 0.5$ instead of $\nu = 1$) in Figure 1.5a. Recent experimental study on MoSe₂/WS₂ heterobilayers by Ciorciaro et. al.³² shows that ferromagnetism is observed between $\nu = 1$ and $\nu = 3/2$. Surprisingly, their results show that ferromagnetism diminishes at van Hove singularity ($\nu = 3/2$). To interpret the aforementioned results, one can define magnetic susceptibilities for antiferromagnetic and ferromagnetic ordering that are given by,⁴²

$$\chi_{\text{AFM}} = \frac{\chi_{\text{Curie}}}{1 + T_c/T} \quad (1.4)$$

$$\chi_{\text{FM}} = \frac{\chi_{\text{Curie}}}{1 - T_c/T} \quad (1.5)$$

where $\chi_{\text{Curie}} \propto 1/T$. Thus, as T increases, $T\chi_{\text{Curie}}$ is constant, $T\chi_{\text{AFM}}$ increases, $T\chi_{\text{FM}}$ decreases. Figure 1.5b shows the susceptibility multiplied by temperature $T\chi$ as a function of filling factor in MoSe₂/WS₂ heterobilayers for three different temperature values.³² For $\nu < 1.0$, the system is paramagnetic because it is temperature dependent. For higher filling between 1.0 and 1.5, the system becomes ferromagnetic where $T\chi$ decreases as temperature T increases. For filling values higher than 3/2, antiferromagnetic behavior is observed as $T\chi$ increases with temperature T . In this study, we investigate this behavior

in finite lattices.

1.4. Wigner crystallization

Wigner crystals are periodic arrangement of localized electrons due to long range correlations.⁴³ At low densities, the average electron separation increases, thereby reducing both kinetic energy and Coulomb repulsion between electrons. As density decreases, the long range Coulomb potential dominates over kinetic energy which eventually becomes negligible. As a result, electrons behave similar to classical point charges separated uniformly, thereby forming a crystal structure.

To show the relation between electron density and energy scales, we consider the effective band Hamiltonian for electrons with effective mass m_{eff} and dielectric permittivity ϵ is given by,⁴⁴

$$H = -\frac{\hbar^2}{2m_{\text{eff}}} \sum_i \nabla_i^2 + \frac{1}{2} \sum_{ij} \frac{1}{4\pi\epsilon} \sum_{ij} \frac{e^2}{|\vec{r}_i - \vec{r}_j|} \quad (1.6)$$

The effective Rydberg energy in terms of ϵ , and in terms of κ is given by,

$$R_y^* = \frac{1}{2} \frac{e^2}{4\pi\epsilon a_B^*} = \frac{\hbar^2}{2m_{\text{eff}}(a_B^*)^2} \quad (1.7)$$

Thus the Hamiltonian becomes,

$$H = -R_y^* (a_B^*)^2 \sum_i \nabla_i^2 + R_y^* (a_B^*) \sum_{ij} \frac{1}{|\vec{r}_i - \vec{r}_j|} \quad (1.8)$$

By scaling the length by using the transformation $\vec{r} \rightarrow \vec{r}/a_{\text{WS}}$, Hamiltonian can be expressed as,

$$H = \frac{R_y^*}{r_s^2} \left(-\sum_i \nabla_i^2 + r_s \sum_{ij} \frac{1}{|\vec{r}_i - \vec{r}_j|} \right) \quad (1.9)$$

where r_s is a dimensionless Wigner-Seitz parameter defined by $r_s = \frac{a_{\text{WS}}}{a_B^*}$ where a_{WS} is Wigner-Seitz radius that corresponds to the average electron separation and a_B^* is effective

Bohr radius given by,

$$a_B^* = \frac{4\pi\epsilon\hbar^2}{m_{\text{eff}}e^2} \quad (1.10)$$

To express the relation between r_s and electron density n , the latter can be described in terms of d -dimensional Wigner-Seitz sphere $V_{\text{WS}}^{(d)}$,

$$n = \frac{N}{V} = \frac{1}{V_{\text{WS}}^{(d)}} \quad (1.11)$$

where N and V are the total number of charges and total volume respectively. For two dimensional systems, $V_{\text{WS}}^{(d)} = \pi a_{\text{WS}}^2$, thus r_s becomes,

$$r_s = \frac{1}{a_B^*} \frac{1}{\sqrt{\pi n}} \quad (1.12)$$

As shown in equation 1.9, both kinetic energy and Coulomb potential decreases by r_s . However, $1/r_s$ dependence of Coulomb potential compared to $1/r_s^2$ dependence of kinetic energy causes this term to dominate for large r_s . For Two Dimensional Electron Gas (2DEG), the crystallization transition occurs around $r_s \approx 30 - 35$.⁴⁵ As equation 1.12 shows, r_s is inversely proportional to the square root of the electron density. Additionally, considering the definition of effective Bohr radius given by equation 1.10, r_s is proportional to the ratio m_{eff}/ϵ . Therefore, r_s can also be tuned by dielectric permittivity ϵ in addition to electron density.

CHAPTER 2

METHODS

In this study, Variational Monte Carlo (VMC) and Diffusion Monte Carlo (DMC) methods will be used to determine ground state of correlated electron systems in Moiré superlattices. Although VMC is computationally more feeble than DMC, the latter is more reliable in terms of the accuracy. They can be used consecutively, i.e. the output of VMC calculation is used as the input for DMC calculation. This way the balance between accuracy and computation cost will be expected.

In VMC calculations, one needs to define the potential that determines carrier dynamics and the trial wave-function which will be briefly described in section 2.4. As for the trial wave-functions, the ground-state wave-functions determined from Mean-Field Hubbard calculations can be used. Because Mean-Field Hubbard (MFH) calculations are based on the Tight-Binding (TB) models, an introduction to the TB model and energy bands is also given as a subsection.

In addition, by implementing moiré potential for finite systems, the edge effects can be probed to reveal interesting physics. Therefore, we implemented a more realistic model which we call Gaussian sum potential.

For numerical modelling of Quantum Monte Carlo Methods, Cornell - Holland Ab-initio Materials Package (CHAMP)⁴⁶ were used for both VMC and DMC simulations. SciPy⁴⁷ and NumPy⁴⁸ packages were used for fitting and diagonalization tasks. The figures are produced via our Python codes by using matplotlib⁴⁹ library.

2.1. Moiré Potential for Finite Lattices

The parameters V_m and ψ of the moiré potential given by eq. 1.1 can be calculated by using the ab initio methods such as Density Functional Theory on bulk heterobilayer TMD materials.^{22,24} Although both the modulation potential V_m and the phase ψ are dependent on the twist angle, the dependence becomes much weaker for small twist angles for which the moiré period is large,²⁴ making them material-dependent properties. Nev-

ertheless, the modulation potential can be modified by applying vertical electric field⁵⁰ and/or applying pressure.³⁶

Because moiré potential given by eq. 1.1 is periodic, the calculations for finite systems will heavily depend on the boundaries of the simulation area. Hence, as an approximation, Gaussian potentials in the form

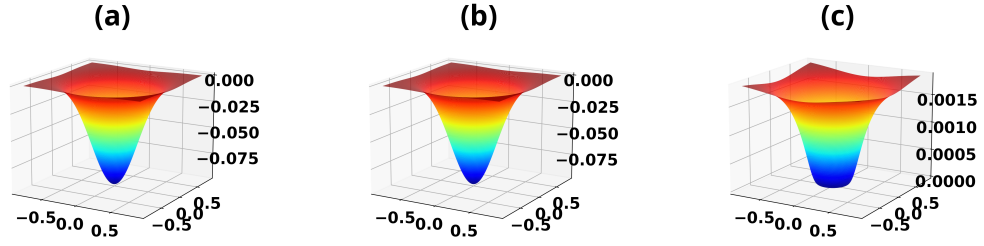
$$V_g(\vec{r}) = \sum_i V_i(\vec{r}) = \sum_i \left(-V_0 \exp \left(- \left(\frac{|\vec{r} - \vec{R}_i|^2}{\rho^2} \right)^s \right) \right) \quad (2.1)$$

can be fitted to the moiré potentials by constraining the shapes of the potentials to the system. \vec{R}_i in Eq. 2.1 denotes the site coordinates. Moiré potentials are different from Gaussian potentials in a manner that the former has three sublattices corresponding to hills, wells and zero-valued midpoints. Therefore, in general, using gaussian wells on a single triangular sublattice can not describe the moiré potential in a finite structure. In addition, the potential must reach the highest value outside of the system to prevent electrons from escaping to eliminate fictitious edge effects on the system. To that end, three different Gaussian-like functions are employed for each sublattice; one corresponding to hills, another to wells and a third to midpoints to define finite moiré potential in terms of the sum over these Gaussians by,

$$V(\vec{r}) = \alpha \left(V_b + \sum_n^{N_{\text{pot}}} \sum_i^{N_{\text{cent}}^n} V_{0,n} \exp \left(- \left(\frac{|\vec{r} - \vec{R}_{n,i}|^2}{\rho_n^2} \right)^{s_n} \right) \right) \quad (2.2)$$

where α is the scale parameter for tuning the potential, V_b is bias to shift, $\vec{R}_{n,i}$ is i^{th} site at n^{th} sublattice. The Gaussians at each sublattice n has an amplitude $V_{0,n}$, a radius ρ_n , and a stiffness s_n . Fig. 2.2b shows such three sublattices in a 7x7 triangular lattice by black, red and green squares as well as the fitted sum of Gaussians. Fig. 2.2c shows that the maximum error is less than 0.5% which occurs at the site centers.

In addition to successful fitting in the bulk, the potential has to be large enough to restrict electronic motion to the system. Our attempts to fit three different Gaussians with positive s_n failed because the resulting potential has minima outside the system. By using a Gaussian-like function with $s_n < 0$ as shown in Fig. 2.1c, the resulting potential has maxima outside the system, i.e. the electronic motion is restricted to the system as shown in Fig. 2.3a.



$v_0=-0.0974, \rho=0.4158, s=1.0205$ $v_0=-0.0959, \rho=0.4135, s=1.0214$ $v_0=0.0019, \rho=0.3769, s=-1.3241$

Figure 2.1. (a), (b) and (c) show Gaussian-like functions that are used in the sum potential (Fig. 2.2) at minima, maxima and midpoints respectively. (a) and (b) are ordinary Gaussians that are slightly curved, i.e. $s \approx 1$, whereas (c) becomes more flat around its center with negative stiffness, differing from Gaussians.

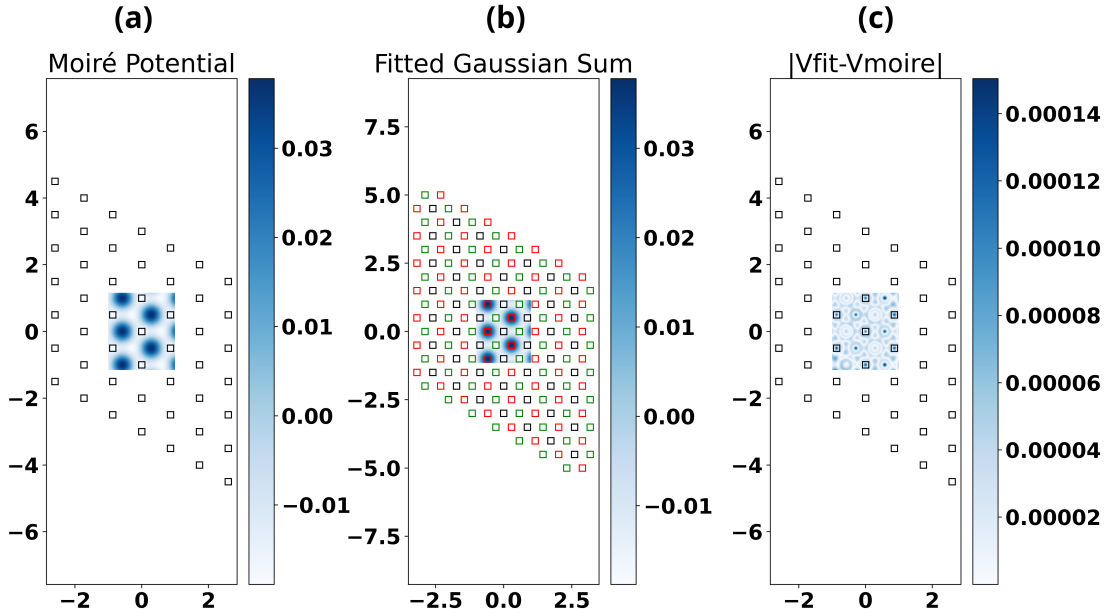


Figure 2.2. (a) Bulk Moiré Potential in a 7×7 triangular lattice given by eq. 1.1 with $V_m = 6.3$ meV and $\psi = 0^\circ$ for MoSe₂/WS₂.³² (b) Finite moiré potential given by eq. 2.2 the fitted to the bulk Moiré potential inside. Black, green and red squares correspond to wells, hills and midpoint sublattices. (c) Absolute difference between fitted potential and moiré potential is shown.

The Gaussian-like function shown in Fig. 2.1c has a singularity at $|\vec{r}|^2 = 0$ because of the negative s_n value. Therefore, a small number 10^{-15} is added to $|\vec{r}|^2$ in our implementation. The potential can further be confined by directional and radial Heaviside step

functions based on logistic function given by,

$$\Theta_{1D}(x) = \frac{1}{1 + \exp(-c(x))} \quad (2.3)$$

where c is the curvature parameter, and x_0 is the center.

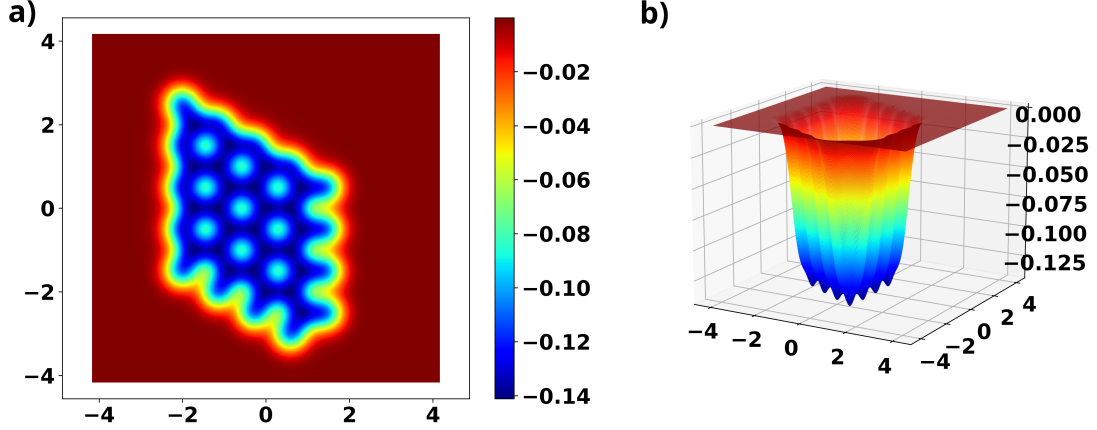


Figure 2.3. Top-view (a) and side-view (b) of the resulting finite moiré potential is shown in eV. Bias V_b is shifted such that the maxima goes to zero outside the system.

In two dimensions, the crossing is defined by a line, beyond which the function is one (or zero on the other side). A line is defined by $y = mx$, and $m = \tan(\phi)$ is the tangent. Thus,

$$\cos(\phi)y = \sin(\phi)x \quad (2.4)$$

and

$$\Theta_{2D}(x, y) = \frac{1}{1 + \exp(c(\sin(\phi)x - \cos(\phi)y))} \quad (2.5)$$

Similarly, by using $m_1 = y/x = \tan(\phi_1)$ and $m_2 = y/z = \tan(\phi_2)$, we can define Θ_{3D} as,

$$\Theta_{3D}(x, y, z) = \frac{1}{1 + \exp(c(\cos(\phi_2)(\sin(\phi_1)x - \cos(\phi_1)y) + \sin(\phi_2)z))} \quad (2.6)$$

Additionally, d -dimensional radial Heaviside step function can be defined by,

$$\Theta_{\text{rad}}(\vec{r}, R) = \frac{1}{1 + \exp\left(c \left(\left[\sum_{i=1}^d (\hat{e}_i \cdot \vec{r})^2\right] - R^2\right)\right)} \quad (2.7)$$

where $\hat{e}_i \cdot \vec{r}$ is the projection of \vec{r} on the unit vector \hat{e}_i . The total potential in terms of Gaussian sum $V_{\text{gs}}(\vec{r})$ and an arbitrary number of Heaviside step functions is given by

$$V_{\text{total}}(\vec{r}) = V_{\text{gs}}(\vec{r}) \prod_{n=1}^{N_{\text{hsf}}} \Theta_n(\vec{r} - \vec{r}_{0,n}) \quad (2.8)$$

where N_{hsf} is the number of predefined Heaviside step functions and $\vec{r}_{0,n}$ is the center of n^{th} HSF. These functions were implemented in CHAMP software package⁴⁶ to be used along with finite moiré potential.

2.2. Tight-Binding Model

In real crystals, the electronic motion is determined by the crystal potential which has pockets with minima at the position of each ion, caused by the Coulomb interaction between the electrons and positively charged ions. As an approximation, Tight-Binding (TB) model assumes that the valence electrons are bound to the atoms which can hop to the neighbor atoms.⁵¹ Therefore, the electronic wave-functions can be described by a superposition of these localized orbitals. Although atomic orbitals are the simplest choice of the basis set, they do not necessarily form an orthonormal basis. Alternatively, one can use Wannier functions which form an orthonormal basis that are composed of linear combinations of atomic orbitals. As simple example, consider two atoms bound to each other in vacuum (see Fig. 2.4a), having different potentials at each atom. The tight binding Hamiltonian of such system is given by,

$$H_1 = \mathcal{E}_1 \hat{a}_1^\dagger \hat{a}_1 + \mathcal{E}_2 \hat{a}_2^\dagger \hat{a}_2 + t(\hat{a}_1^\dagger \hat{a}_2 + \hat{a}_2^\dagger \hat{a}_1) \quad (2.9)$$

where \mathcal{E}_1 and \mathcal{E}_2 are the on-site energies (i.e. the site potentials), t is the hopping strength between the nearest neighbors and \hat{a}_j (\hat{a}_j^\dagger) are the annihilation (creation) operators for the first and the second atomic states $|1\rangle$ and $|2\rangle$, \dagger denotes the Hermitian conjugation. See

Sakurai & Napolitano³⁹ for further information about operator formulation of quantum mechanics.

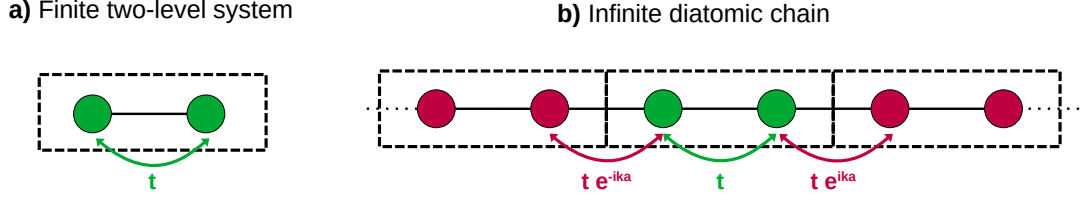


Figure 2.4. (a) Finite two-level system in which two atoms are coupled to each other with a hopping amplitude t . (b) Infinite diatomic chain with consists of two atoms per unit cell with nearest-neighbor coupling.

To focus on introducing the elementary concepts, we ignore spin and represent the equations in matrix form. The matrix form the Hamiltonian and the state vectors can be represented by,

$$H = \begin{bmatrix} \mathcal{E}_1 & -t \\ -t & \mathcal{E}_2 \end{bmatrix}, \quad |1\rangle = \begin{bmatrix} 1 \\ 0 \end{bmatrix}, \quad |2\rangle = \begin{bmatrix} 0 \\ 1 \end{bmatrix} \quad (2.10)$$

By diagonalizing the Hamiltonian matrix given by Eq. 2.9 we obtain the eigenvalues of the Hamiltonian which provides the energy levels of the system,

$$E_{\pm} = \frac{\mathcal{E}_1 + \mathcal{E}_2}{2} \pm \frac{1}{2} \sqrt{(\delta\mathcal{E})^2 + 4t^2} \quad (2.11)$$

where $\delta\mathcal{E} = \mathcal{E}_2 - \mathcal{E}_1$. We can also form an infinite chain by using the two-level system as the unit cell by introducing Bloch periodicity,⁵¹

$$H(k) = \begin{bmatrix} \mathcal{E}_1 & t (1 + \exp(-ika)) \\ t (1 + \exp(ika)) & \mathcal{E}_2 \end{bmatrix} \quad (2.12)$$

where k is the wave-number along one dimension (called wave-vector in higher dimensions) and a is the lattice constant. Such system is shown in Fig. 2.4b.

The Bloch terms (i.e. $\exp(\pm ika)$) represent the coupling between the atoms to the neighbor unit cells. The detailed description of Bloch's theorem is given by.⁵¹ The idea is

based on the periodic nature of the crystal potential which causes wave-functions to have the same periodicity as the potential. The Hamiltonian for this diatomic chain becomes k -dependent as well as its energy levels,

$$E_{\pm}(k) = \frac{\mathcal{E}_1 + \mathcal{E}_2}{2} \pm \frac{1}{2} \sqrt{(\delta\mathcal{E})^2 + 8t^2(1 + \cos(ka))} \quad (2.13)$$

where $E_{\pm}(k)$ are called band energies. A sample calculation for $t = 1$, $\mathcal{E}_1 = 0$ and $\mathcal{E}_2 = 1$ is shown in Fig. 2.5a.

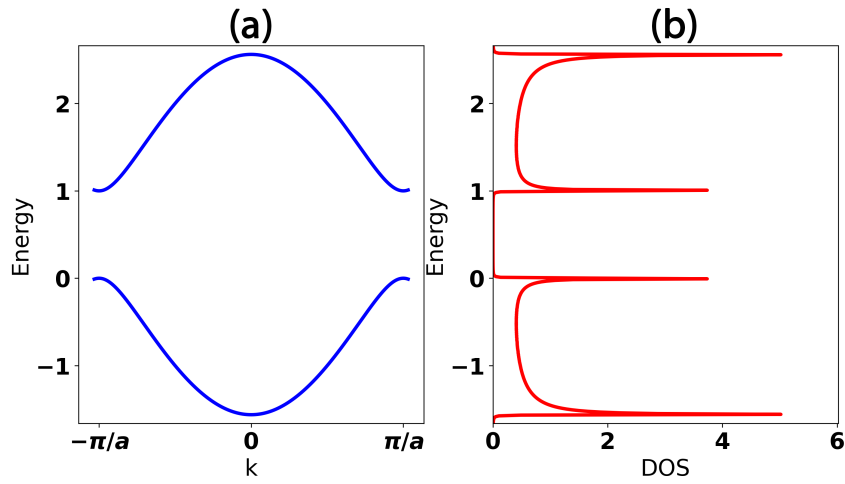


Figure 2.5. (a) Energy band diagram and (b) density of states of diatomic chain shown in Fig. 2.4.

For a triangular lattice shown in Fig. 2.6a, the lattice vectors are given by,

$$\vec{a}_1 = a\hat{y}, \quad \vec{a}_2 = \frac{\sqrt{3}}{2}a\hat{x} - \frac{1}{2}a\hat{y} \quad (2.14)$$

where a is the lattice constant. The corresponding reciprocal lattice vectors are given by,

$$\vec{b}_1 = \frac{4\pi}{\sqrt{3}a} \left(\frac{1}{2}\hat{x} + \frac{\sqrt{3}}{2}\hat{y} \right), \quad \vec{b}_2 = \frac{4\pi}{\sqrt{3}a}\hat{x} \quad (2.15)$$

The reciprocal lattice is shown in Fig. 2.6b with high-symmetry points. The corresponding energy bands can be calculated by using the nearest neighbor displacement

vectors δ and the corresponding hopping parameters t_δ ,

$$\mathcal{E}(\vec{k}) = \sum_{\vec{\delta}} -t_{\vec{\delta}} e^{i\vec{k}\cdot\vec{\delta}} = -t \sum_{s=0}^1 \left\{ e^{(-1)^s i\vec{k}\cdot\vec{a}_1} + e^{(-1)^s i\vec{k}\cdot\vec{a}_2} + e^{(-1)^s i\vec{k}\cdot(\vec{a}_1+\vec{a}_2)} \right\} \quad (2.16)$$

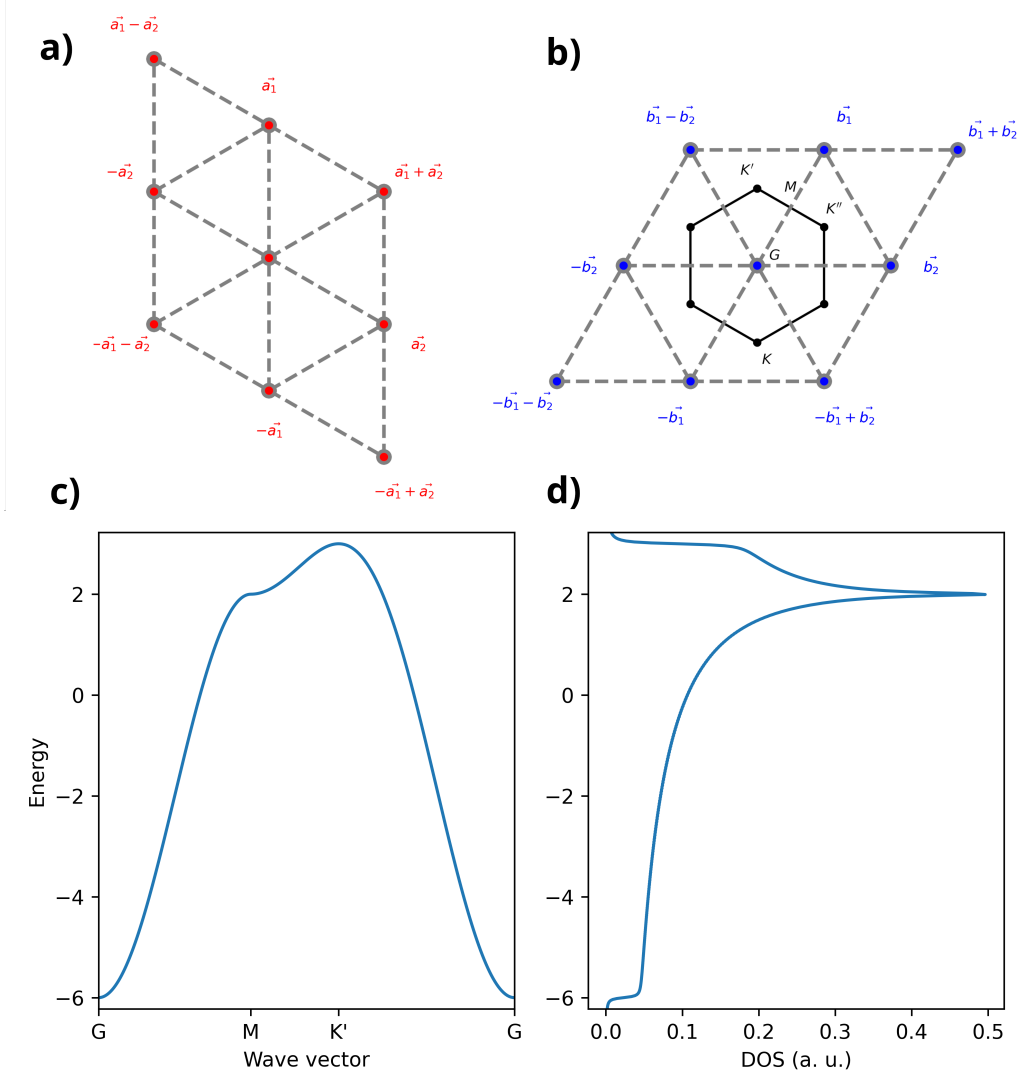


Figure 2.6. (a) Triangular lattice site in the center and its neighbors translated by $n\vec{a}_1 + m\vec{a}_2$ with $n, m \in 0, \pm 1$, and (b) the reciprocal lattice site in the center and its neighbors translated by $n\vec{b}_1 + m\vec{b}_2$ with $n, m \in 0, \pm 1$ are shown. The first Brillouin zone is shown by black hexagon, and high-symmetry points are annotated by black symbols. (c) Energy band diagram and (d) density of states are also shown.

The resulting energy band dispersion becomes,

$$\mathcal{E}(\vec{k}) = -2t \cos(k_y a) - 4t \cos\left(\frac{\sqrt{3}}{2} k_x a\right) \cos\left(\frac{k_y a}{2}\right) \quad (2.17)$$

The band energies with respect to the wave-vectors along high-symmetry points (see Fig. 2.6b) is shown in Fig. 2.6.

Apart from band diagrams, there is another quantity called Density of States (DOS) that reveals essential information such as localization and band gap. The density of states is defined as a function of energy is given by,⁵¹

$$\mathcal{D}(E) = \sum_n \delta(E - \mathcal{E}_n) \quad (2.18)$$

$$\mathcal{D}(E) = \sum_n \int \frac{d^3 \vec{k}}{(2\pi)^3} \delta(E - \mathcal{E}_{n,\vec{k}}) \quad (2.19)$$

where Eq. 2.18 is for finite systems while Eq. 2.19 is for periodic systems that involves an integral over \vec{k} . DOS can also be expressed by using Green's functions,⁵¹

$$\mathcal{D}(E) = -\frac{1}{\pi} \text{Im} \left[\sum_n \langle n | \widehat{G}_\eta(E) | n \rangle \right] \quad (2.20)$$

$$\mathcal{D}(E) = -\frac{1}{\pi} \text{Im} \left[\sum_n \int \frac{d^3 \vec{k}}{(2\pi)^3} \langle n | \widehat{G}_\eta(\vec{k}, E) | n \rangle \right] \quad (2.21)$$

with the operator forms of Green's functions,

$$\widehat{G}_\eta(E) = (\widehat{H} - (E + i\eta) \widehat{I})^{-1} \quad (2.22)$$

$$\widehat{G}_\eta(\vec{k}, E) = (\widehat{H}(\vec{k}) - (E + i\eta) \widehat{I})^{-1} \quad (2.23)$$

where $\widehat{I} = \sum_n |n\rangle \langle n|$ is the identity operator and η is a small positive number to prevent singularities in extremely localized systems such as two-level system shown in 2.4a. The formula given by Eq. 2.22 and Eq. 2.23 are based on the definition of $\delta(x)$,⁵¹

$$\delta(x) = \frac{1}{\pi} \frac{\eta}{x^2 + \eta^2} \quad (2.24)$$

In matrix notation, the Green's function can be computed by using Eq. 2.22 and Eq. 2.23 to evaluate DOS by computing its trace, and it is integrated over \vec{k} if the system

is periodic.

Additionally, the eigenvalues of the Hamiltonian can be used to evaluate Eq. 2.18 and Eq. 2.19. However, the states are extremely localized for finite systems and exact numerical treatment of delta functions is not well-defined, so we can introduce broadening by using the definition of delta function given by Eq. 2.24,

$$\mathcal{D}(E) = \frac{1}{\pi} \sum_n \frac{\eta}{(E - \mathcal{E}_n)^2 + \eta^2} \quad (2.25)$$

$$\mathcal{D}(E) = \frac{1}{\pi} \sum_n \int \frac{d^3\vec{k}}{(2\pi)^3} \frac{\eta}{(E - \mathcal{E}_{n,\vec{k}})^2 + \eta^2} \quad (2.26)$$

where equations 2.25 and 2.26 are for finite and periodic systems respectively. DOS of diatomic chain and triangular lattice are shown in Fig. 2.5b and Fig. 2.6d respectively. The singularities appearing in density of states at the extrema of corresponding band energies are called Van-Hove singularities.⁵¹ Van Hove singularities are important in terms of electron correlation especially in narrow-band systems such as twisted bilayer graphene⁵² and heterobilayer TMDs.^{10,11,22,24,53}

In general, one can fit tight-binding parameters to the bands that are obtained empirically or via ab Initio calculations such as Density Functional Theory (DFT) calculations. Accuracy of the fitted TB model can be improved by adding second, third and further nearest neighbor interactions to the Hamiltonian.

One of the most successful examples of TB models is graphene⁵⁴ which forms a honeycomb crystal that can be modeled with a triangular lattice with two atoms per unit cell. The 2s, 2p_x and 2p_y orbitals of each carbon atom in graphene are hybridized, forming an sp²-type hybridization. The hybridized orbitals have lower energies than the remaining 2p_z orbital and the electrons in former orbitals are bound more tightly than the latter. As a result, 2p_z electrons contribute to the conduction, and the tight-binding model using orthogonalized 2p_z orbitals as orthonormal basis successfully capture band linearity at charge neutrality. In a similar way, one band Hubbard models of moiré heterostructures are based on single orbital tight-binding models.²²

2.3. Mean-Field Hubbard Model

Tight-binding model is an approximation for studying single electrons in non-interacting systems. The exact ground state energies of non-interacting systems can be studied by using Density Functional Theory (DFT) which minimizes energy functional of the electron density.⁵⁵ In both DFT and tight-binding models, the electron correlation is not taken into account intrinsically. Although electron correlations can be approximated by exchange-correlation functionals in DFT, the exact estimation of ground state is possible with quantum Monte Carlo methods.⁵⁵

An approximate estimation of the ground-state of a correlating system can be calculated by solving the self-consistent mean-field Hubbard model starting with a tight-binding Hamiltonian. The general form of the many-body Hamiltonian is given by,⁴⁴

$$H_{\text{MB}} = -\frac{\hbar^2}{2m} \sum_j \nabla_j^2 + \sum_{i,j} V_{\text{eff}}^j(\vec{r}_i - \vec{R}_j) + \frac{1}{2} \frac{1}{4\pi\epsilon_0} \sum_{i,j} \frac{1}{|\vec{r}_i - \vec{r}_j|} \quad (2.27)$$

where the first term is the kinetic energy of electrons, the second term is the screened Coulomb interaction between electrons and ions and the last term corresponds to Coulomb interaction between electrons. The 1/2 factor in the last term is to prevent double counting in the summation.

To incorporate Coulomb interaction, one first needs to define many-body wave-function by using second quantization. In second-quantized formulation, the field operators (or many-body wave-functions) are defined by using the orthogonal eigenstates $\phi(\vec{r})$ of the Hamiltonian,^{44,56}

$$\Phi(\vec{r}) = \sum_{j\sigma} \hat{c}_{j\sigma} \phi_j(\vec{r}) \quad (2.28)$$

$$\Phi^\dagger(\vec{r}) = \sum_{j\sigma} \hat{c}_{j\sigma}^\dagger \phi_j(\vec{r}) \quad (2.29)$$

where $\hat{c}_{j\sigma}$ ($\hat{c}_{j\sigma}^\dagger$) are the annihilation (creation) operators which destroys (creates) an electron with spin σ at orbital j . The second-quantized forms of the spin dependent annihilation and creation operators are given by $\hat{c}_{j\sigma}$ and $\hat{c}_{j\sigma}^\dagger$ which destroys or creates an electron at j^{th} orbital with spin σ . The order of the operators is important when applying the creation or annihilation operators consecutively. The first two terms of the Hamiltonians

correspond to tight-binding which can be represented in second-quantized formalism by,

$$\begin{aligned}
\widehat{H}_0 &= \int d^3\vec{r} \Phi^\dagger(\vec{r}) \widehat{H}_0 \Phi(\vec{r}) \\
&= \sum_{i,j,\sigma,\sigma'} \hat{c}_{i\sigma}^\dagger \hat{c}_{j\sigma'} \int d^3\vec{r} \phi_i^*(\vec{r}) \widehat{H}_0 \phi_j(\vec{r}) \\
&= \sum_{i\sigma} \mathcal{E}_i \hat{c}_{i\sigma}^\dagger \hat{c}_{i\sigma} + \sum_{\langle i,j \rangle, \sigma} \left(t_{ij} \hat{c}_{i\sigma}^\dagger \hat{c}_{j\sigma} + t_{ij}^* \hat{c}_{j\sigma}^\dagger \hat{c}_{i\sigma} \right) \quad (2.30)
\end{aligned}$$

where we used the fact that the integral does not vanish only if i and j are equal or nearest-neighbors, however, derivations of higher range hopping terms are straightforward. The annihilation and creation operators in the first term have the same indices which means that an electron in an orbital is destroyed before an electron is created in the same orbital and \mathcal{E}_i corresponds to the energy cost of this operation. Similarly, the second term involves consecutive destruction and creation of neighbor atoms and t_{ij} corresponds to the energy cost of the scattering between neighbor atoms. These two terms correspond to the lattice hopping which is independent of spin. The second-quantized representation of Coulomb interaction in Eq. 2.27 is two-body scattering is given by,^{44,56}

$$\widehat{V}_C = \frac{1}{2} \sum_{i,j} \frac{1}{4\pi\epsilon_0} \frac{1}{|\vec{r}_i - \vec{r}_j|} \quad (2.31)$$

$$= \frac{1}{2} \sum_{\substack{ijkl \\ \sigma\sigma'}} V_{ijkl} \hat{c}_{i\sigma}^\dagger \hat{c}_{j\sigma'}^\dagger \hat{c}_{k\sigma'} \hat{c}_{l\sigma} \quad (2.32)$$

with,

$$V_{ijkl} = \int d^3\vec{r}_1 \int d^3\vec{r}_2 \phi_i^\dagger(\vec{r}_1) \phi_j^\dagger(\vec{r}_2) \frac{1}{4\pi\epsilon_0} \frac{1}{|\vec{r}_1 - \vec{r}_2|} \phi_k(\vec{r}_2) \phi_l(\vec{r}_1) \quad (2.33)$$

where \vec{r}_1 and \vec{r}_2 are the coordinates of two electrons that are involved in scattering. The summation involves multiple types of scatterings between orbitals i, j, k and l . They satisfy anti-commutation relations given by,

$$\{\hat{c}_{i\sigma}, \hat{c}_{j\sigma'}\} = 0, \quad \{\hat{c}_{i\sigma}^\dagger, \hat{c}_{j\sigma'}^\dagger\} = 0, \quad \{\hat{c}_{i\sigma}, \hat{c}_{j\sigma'}^\dagger\} = \delta_{ij} \delta_{\sigma\sigma'} \quad (2.34)$$

where the anti-commutators are defined by $\{\widehat{A}, \widehat{B}\} = \widehat{A}\widehat{B} + \widehat{B}\widehat{A}$ and δ_{ij} is Kronecker delta

function given by

$$\delta_{ij} = \begin{cases} 0 & i \neq j \\ 1 & i = j \end{cases} \quad (2.35)$$

Additionally, we can introduce the number operator given by $\hat{n}_{i\sigma} = \hat{c}_{i\sigma}^\dagger c_{i\sigma}$ which returns the number of electrons of spin σ at orbital i . To derive Hubbard Hamiltonian we first need to rearrange Coulomb term given by Eq. 2.33 by using the anti-commutator relations,

$$\hat{c}_{k\sigma'} \hat{c}_{l\sigma} = -\hat{c}_{l\sigma} \hat{c}_{k\sigma'} \quad (2.36)$$

$$\hat{c}_{j\sigma'}^\dagger \hat{c}_{l\sigma} = \delta_{jl} \delta_{\sigma\sigma'} - \hat{c}_{l\sigma} \hat{c}_{j\sigma'}^\dagger \quad (2.37)$$

$$\widehat{V}_C = \frac{1}{2} \sum_{\substack{ijkl \\ \sigma\sigma'}} V_{ijkl} \left(\hat{c}_{i\sigma}^\dagger \left(\hat{c}_{l\sigma} \hat{c}_{j\sigma'}^\dagger - \delta_{jl} \delta_{\sigma\sigma'} \right) \hat{c}_{k\sigma'} \right) \quad (2.38)$$

$$= \frac{1}{2} \sum_{\substack{ijkl \\ \sigma\sigma'}} V_{ijkl} \left(\hat{c}_{i\sigma}^\dagger \hat{c}_{l\sigma} \hat{c}_{j\sigma'}^\dagger \hat{c}_{k\sigma'} - \delta_{jl} \delta_{\sigma\sigma'} c_{i\sigma}^\dagger \hat{c}_{k\sigma} \right) \quad (2.39)$$

$$= \frac{1}{2} \sum_{\substack{ijkl \\ \sigma\sigma'}} V_{ijkl} \hat{c}_{i\sigma}^\dagger \hat{c}_{l\sigma} \hat{c}_{j\sigma'}^\dagger \hat{c}_{k\sigma'} - \frac{1}{2} \sum_{ijk\sigma} V_{ijkj} \hat{c}_{i\sigma}^\dagger \hat{c}_{k\sigma} \quad (2.40)$$

In the lowest order approximation, only the interactions at the same orbital are taken into account, i.e. $i = j = k = l$ and the potential of this interaction is defined by $U = V_{iiii}$,

$$\widehat{V}_C = \frac{U}{2} \sum_{i\sigma\sigma'} \hat{c}_{i\sigma}^\dagger \hat{c}_{i\sigma} \hat{c}_{i\sigma'}^\dagger \hat{c}_{i\sigma'} - \frac{U}{2} \sum_{i\sigma} c_{i\sigma}^\dagger \hat{c}_{i\sigma} \quad (2.41)$$

We can expand this summation by substituting spins $\sigma \in \{\uparrow, \downarrow\}$ and number operators $\hat{n}_{i\sigma} = \hat{c}_{i\sigma}^\dagger c_{i\sigma}$ into \widehat{V}_C ,

$$\widehat{V}_C = \frac{1}{2} \sum_i U \left(\hat{n}_{i\uparrow} \hat{n}_{i\uparrow} + \hat{n}_{i\uparrow} \hat{n}_{i\downarrow} + \hat{n}_{i\downarrow} \hat{n}_{i\uparrow} + \hat{n}_{i\downarrow} \hat{n}_{i\downarrow} - \hat{n}_{i\uparrow} - \hat{n}_{i\downarrow} \right) \quad (2.42)$$

$$= \frac{U}{2} \sum_i \left(\hat{n}_{i\uparrow} (\hat{n}_{i\uparrow} - 1) + \hat{n}_{i\downarrow} (\hat{n}_{i\downarrow} - 1) + \hat{n}_{i\uparrow} \hat{n}_{i\downarrow} + \hat{n}_{i\downarrow} \hat{n}_{i\uparrow} \right) \quad (2.43)$$

since the occupations $n_{i\sigma} \in \{0, 1\}$ the first two terms in the summation becomes zero,

therefore the Hubbard Hamiltonian $\widehat{H} = \widehat{H}_0 + \widehat{V}_C$ (see Eq. 2.30) becomes,

$$\widehat{H} = \sum_{i\sigma} \mathcal{E}_{i\sigma} \hat{n}_{i\sigma} + \sum_{\langle i,j \rangle, \sigma} t_{ij} \left(\hat{c}_{i\sigma}^\dagger \hat{c}_{j\sigma} + \hat{c}_{j\sigma}^\dagger \hat{c}_{i\sigma} \right) + \frac{U}{2} \sum_i (\hat{n}_{i\uparrow} \hat{n}_{i\downarrow} + \hat{n}_{i\downarrow} \hat{n}_{i\uparrow}) \quad (2.44)$$

where the hopping amplitude t_{ij} is a real number. In mean-field approximation, the number operators are expressed in terms of their mean values,

$$\hat{n}_{i\uparrow} = \langle \hat{n}_{i\uparrow} \rangle + (\hat{n}_{i\uparrow} - \langle \hat{n}_{i\uparrow} \rangle) \quad (2.45)$$

$$\hat{n}_{i\downarrow} = \langle \hat{n}_{i\downarrow} \rangle + (\hat{n}_{i\downarrow} - \langle \hat{n}_{i\downarrow} \rangle) \quad (2.46)$$

by ignoring the smallest terms $(\hat{n}_{i\uparrow} - \langle \hat{n}_{i\uparrow} \rangle)(\hat{n}_{i\downarrow} - \langle \hat{n}_{i\downarrow} \rangle)$ the Hamiltonian becomes,

$$\widehat{H}_{\text{MF}} = \sum_{i\sigma} \mathcal{E}_{i\sigma} \hat{c}_{i\sigma}^\dagger \hat{c}_{i\sigma} + \sum_{\langle i,j \rangle, \sigma} t_{ij} \left(\hat{c}_{i\sigma}^\dagger \hat{c}_{j\sigma} + \hat{c}_{j\sigma}^\dagger \hat{c}_{i\sigma} \right) \quad (2.47)$$

$$+ U \sum_i (\langle \hat{n}_{i\uparrow} \rangle \hat{n}_{i\downarrow} + \langle \hat{n}_{i\downarrow} \rangle \hat{n}_{i\uparrow} - \langle \hat{n}_{i\uparrow} \rangle \langle \hat{n}_{i\downarrow} \rangle) \quad (2.48)$$

For a spin-unpolarized system, i.e. $\langle n_{i\uparrow} \rangle = \langle n_{i\downarrow} \rangle = 1/2$, we can define $\widehat{H}_{\text{MF}}^0$ by,⁵⁷

$$\widehat{H}_{\text{MF}}^0 = \sum_{i\sigma} \mathcal{E}_{i\sigma} \hat{c}_{i\sigma}^\dagger \hat{c}_{i\sigma} + \sum_{\langle i,j \rangle, \sigma} t_{ij} \left(\hat{c}_{i\sigma}^\dagger \hat{c}_{j\sigma} + \hat{c}_{j\sigma}^\dagger \hat{c}_{i\sigma} \right) + \frac{U}{2} \sum_i \left(\hat{n}_{i\downarrow} + \hat{n}_{i\uparrow} - \frac{1}{2} \right) \quad (2.49)$$

$$= \sum_{i\sigma} \mathcal{E}'_{i\sigma} \hat{c}_{i\sigma}^\dagger \hat{c}_{i\sigma} + \sum_{\langle i,j \rangle, \sigma} t_{ij} \left(\hat{c}_{i\sigma}^\dagger \hat{c}_{j\sigma} + \hat{c}_{j\sigma}^\dagger \hat{c}_{i\sigma} \right) \quad (2.50)$$

where $\mathcal{E}'_{i\sigma} = \mathcal{E}_{i\sigma} + \frac{U}{4}$ and rewrite \widehat{H}_{MF} as,

$$\widehat{H}_{\text{MF}} = \widehat{H}_{\text{MF}} - \widehat{H}_{\text{MF}}^0 + \widehat{H}_{\text{MF}}^0 \quad (2.51)$$

$$= \sum_{i\sigma} \mathcal{E}_{i\sigma} \hat{c}_{i\sigma}^\dagger \hat{c}_{i\sigma} + \sum_{\langle i,j \rangle, \sigma} t_{ij} \left(\hat{c}_{i\sigma}^\dagger \hat{c}_{j\sigma} + \hat{c}_{j\sigma}^\dagger \hat{c}_{i\sigma} \right) + U \sum_i (\langle \hat{n}_{i\uparrow} \rangle \hat{n}_{i\downarrow} + \langle \hat{n}_{i\downarrow} \rangle \hat{n}_{i\uparrow} - \langle \hat{n}_{i\uparrow} \rangle \langle \hat{n}_{i\downarrow} \rangle) \quad (2.52)$$

$$- \sum_{i\sigma} \mathcal{E}_{i\sigma} \hat{c}_{i\sigma}^\dagger \hat{c}_{i\sigma} - \sum_{\langle i,j \rangle, \sigma} t_{ij} \left(\hat{c}_{i\sigma}^\dagger \hat{c}_{j\sigma} + \hat{c}_{j\sigma}^\dagger \hat{c}_{i\sigma} \right) - \frac{U}{2} \sum_i \left(\hat{n}_{i\downarrow} + \hat{n}_{i\uparrow} - \frac{1}{2} \right) \quad (2.53)$$

$$+ \sum_{i\sigma} \mathcal{E}'_{i\sigma} \hat{c}_{i\sigma}^\dagger \hat{c}_{i\sigma} + \sum_{\langle i,j \rangle, \sigma} t_{ij} \left(\hat{c}_{i\sigma}^\dagger \hat{c}_{j\sigma} + \hat{c}_{j\sigma}^\dagger \hat{c}_{i\sigma} \right) \quad (2.54)$$

$$= \sum_{i\sigma} \mathcal{E}'_{i\sigma} \hat{c}_{i\sigma}^\dagger \hat{c}_{i\sigma} + \sum_{\langle i,j \rangle, \sigma} t_{ij} \left(\hat{c}_{i\sigma}^\dagger \hat{c}_{j\sigma} + \hat{c}_{j\sigma}^\dagger \hat{c}_{i\sigma} \right)$$

$$+ U \sum_i \left(\left(\langle \hat{n}_{i\uparrow} \rangle - \frac{1}{2} \right) \hat{n}_{i\downarrow} + \left(\langle \hat{n}_{i\downarrow} \rangle - \frac{1}{2} \right) \hat{n}_{i\uparrow} \right) + U \sum_i \langle \hat{n}_{i\uparrow} \rangle \langle \hat{n}_{i\downarrow} \rangle \quad (2.55)$$

where the last term is a constant which can be incorporated into $\mathcal{E}'_{i\sigma}$. By denoting $\mathcal{E}'_{i\sigma}$ as $\mathcal{E}_{i\sigma}$, we can finally write the final form of mean-field Hubbard Hamiltonian

$$\begin{aligned} \hat{H}_{\text{MFH}} = & \sum_{i\sigma} \mathcal{E}_{i\sigma} \hat{c}_{i\sigma}^\dagger \hat{c}_{i\sigma} + \sum_{\langle i,j \rangle, \sigma} t_{ij} \left(\hat{c}_{i\sigma}^\dagger \hat{c}_{j\sigma} + \hat{c}_{j\sigma}^\dagger \hat{c}_{i\sigma} \right) \\ & + U \sum_i \left(\left(\langle \hat{n}_{i\uparrow} \rangle - \frac{1}{2} \right) \hat{n}_{i\downarrow} + \left(\langle \hat{n}_{i\downarrow} \rangle - \frac{1}{2} \right) \hat{n}_{i\uparrow} \right) \end{aligned} \quad (2.56)$$

By using Equation 2.56, the mean-field Hamiltonians for individual spins can be written, and solve self-consistently since the spin-up (spin-down) Hamiltonians depend on the spin-down (spin-up) densities $\langle \hat{n}_{i\downarrow} \rangle$ ($\langle \hat{n}_{i\uparrow} \rangle$).

In this study, a python code for Hubbard calculations was developed for the calculations. The code utilizes several parts to achieve the correct ground state efficiently. The main algorithm in a simplified form is given by algorithm 2.1.

Algorithm 2.1. Self-Consistent Mean-Field Hubbard algorithm

- 1: Set H_\uparrow and H_\downarrow equal to the tight-binding Hamiltonian H_{TB}
 - 2: Calculate eigenvectors ψ_\uparrow and ψ_\downarrow from H_\uparrow and H_\downarrow
 - 3: Calculate initial density matrices by using $D_\sigma = \psi_\sigma \psi_\sigma^\dagger$, where $\langle \hat{n}_{i\sigma} \rangle = \langle i | D_\sigma | i \rangle$
 - 4: Update H_σ by using D_σ
 - 5: Calculate the initial total energy
 - 6: **for** each self-consistent iteration **do**
 - 7: Calculate electron densities D'_σ from H_σ
 - 8: Mix old and new density matrices $D_\sigma \leftarrow (1 - p)D'_\sigma + pD_\sigma$
 - 9: update H_σ and calculate the total energy and check for convergence
 - 10: **if** convergence is achieved or maximum number of iterations is exceeded **then**
 - 11: End program and return H_σ and D_σ
 - 12: **end if**
 - 13: **end for**
-

The success of the algorithm depends on several factors such as the quality of the initial guess, mixing factor p and the number of iterations and convergence criteria. Depending on these factors the calculation may converge to a local minima rather than the global minimum or convergence may not be achieved at all.

To solve the problem with the initial guess, a random sampling on the on-site en-

ergies are introduced,

$$\mathcal{E}_{i\uparrow} = \mathcal{E}_i^0 + R_i \quad (2.57)$$

$$\mathcal{E}_{i\downarrow} = \mathcal{E}_i^0 - R_i \quad (2.58)$$

where R_i are the random numbers such that $R_i \in [0, W/2]$. The random configurations are only used to obtain initial density matrices for the main calculation. The main calculation is performed by using tight-binding Hamiltonian with onsite energies \mathcal{E}_i^0 . By scanning multiple random initial guesses the convergence is improved significantly in exchange for computation time.

The mixing values are important for the determination of correct ground state, so performing calculations over several mixing values is often necessary. To reduce the computation cost, an adaptive mixing was introduced, i.e. the mixing factor changes depending on the convergence behavior. The algorithm is given by Algorithm 2.2.

Algorithm 2.2. Adaptive mixing algorithm for self-consistent MFH calculations

```

1: ...
2:  $k \leftarrow 1$ 
3: for each self-consistent iteration do
4:   ...
5:   if more than half of the last  $N_{\text{adapt}}$  iterations are convergent then
6:      $k \leftarrow (1 - \gamma)k$ 
7:   else
8:      $k \leftarrow (1 + \gamma)k$ 
9:   end if
10:   $p \leftarrow \max(p_{\min}, \min(kp, p_{\max}))$ 
11:  if  $p == p_{\min}$  or  $p == p_{\max}$  then
12:     $k \leftarrow 1$ 
13:  end if
14:  ...
15: end for
16: ...

```

In Algorithm 2.2, k is the coefficient which determines how mixing factor p changes, and γ is a small number to specify how fast k changes. The statement at Line 10 of Alg. 2.2 ensures that p stays in $[p_{\min}, p_{\max}]$. Line 12 of Alg. 2.2 performs a reinitialization of k if p reaches p_{\min} or p_{\max} . The need for $p_{\min} > 0$ and $p_{\max} < 1$ is to prevent the updated densities becoming the same as those of previous iteration. Because the only advantage of

this method is to find nearest minima efficiently, the density matrices (and Hamiltonians) should be evolved enough before the adaptive mixing calculation.

By performing self-consistent calculation for relatively small number of iterations (not necessarily convergent) for multiple mixing values, we can choose the density matrices and Hamiltonians which correspond to minimum total energy as our initial guess which is called relaxation step. At this point, we can choose continuing with whether adaptive mixing or constant mixing, by starting from the mixing value determined from the relaxation step.

With these improvements, the code developed in this study determines initial guess from both tight-binding wave-functions and a given number of random configurations with a given width W which is chosen to be $\approx U$ in our calculations. It performs a relaxation with various mixing values by scanning over initial guess configurations and performs the self-consistent calculation by whether using constant or adaptive mixing on the relaxed Hamiltonians.

2.4. Variational Monte Carlo Method

In Variational Monte Carlo (VMC) method, the variational energy E_v for a non-normalized wave-function Ψ is defined by,^{58,59}

$$E_v = \frac{\langle \Psi | \hat{H} | \Psi \rangle}{\langle \Psi | \Psi \rangle} = \frac{\int d\vec{R} \Psi(\vec{R})^2 E_L(\vec{R})}{\int d\vec{R} \Psi(\vec{R})^2}, \quad E_L = \frac{\hat{H}\Psi(\vec{R})}{\Psi(\vec{R})} \quad (2.59)$$

where ψ is the many-electron wave-function and E_L is the local energy. The derivation is easy for the definitions below,

$$I = \int d\vec{R} |R\rangle \langle R|, \quad \Psi(\vec{R}) = \langle \vec{R} | \Psi \rangle = \Psi^*(\vec{R}) \quad (2.60)$$

Variational energy E_v can be calculated by Monte Carlo sampling technique from a probability distribution $\rho(\vec{R})$,

$$E_v = \int d\vec{R} \rho(\vec{R}) E_L(\vec{R}) \approx \frac{1}{M} \sum_{k=1}^M E_L(\vec{R}_k) \quad (2.61)$$

$$\rho(\vec{R}) = \Psi^2(\vec{R}) / \int d\vec{R} \Psi^2(\vec{R}) \quad (2.62)$$

where probability density $\rho(\vec{R})$ is sampled by Metropolis-Hastings algorithm. The wave function in general has the form,

$$\Psi(\vec{R}) = J(\vec{R})\Phi(\vec{R}) \quad (2.63)$$

where $J(\vec{R})$ is the Jastrow factor which has the information about electron correlation while $\Phi(\vec{R})$ is the Slater determinant. Jastrow factor in equation 2.63 has the form $J(\vec{R}) \propto e^{f(\vec{R})}$.^{58,59}

In most simulations, $f(\vec{R})$ can be chosen as,⁵⁸

$$f(\vec{R}) = \sum_{i=1}^N \chi(\vec{r}_i) - \frac{1}{2} \sum_{i=1}^N \sum_{j=1}^N u(\vec{x}_i, \vec{x}_j) \quad (2.64)$$

where the first and the second terms correspond to electron-nucleus and electron-electron correlations respectively. In this study, we use the Jastrow factor that is defined for graphene quantum dots by,⁶⁰

$$J(\vec{R}) = J_{ee}(\vec{R})J_{ed}(\vec{R})J_{eed}(\vec{R}) \quad (2.65)$$

where ee , ed and eed subscripts correspond to electron-electron, electron-dot, electron-electron-dot respectively.

For a trial wavefunction (i.e. predefined Jastrow factor and Slater determinant), VMC algorithm samples the many-body wave function by using Metropolis-Hastings algorithm. At each step, an electron configuration is proposed, then sampled or discarded depending on the detailed balance condition given by,

$$\frac{P_{\text{acc}}(\vec{R}_f|\vec{R}_i)}{P_{\text{acc}}(\vec{R}_i|\vec{R}_f)} = \frac{P_{\text{prop}}(\vec{R}_i|\vec{R}_f)\rho(\vec{R}_f)}{P_{\text{prop}}(\vec{R}_f|\vec{R}_i)\rho(\vec{R}_i)} \quad (2.66)$$

where $P_{\text{acc}}(\vec{R}'|\vec{R})$ is the acceptance probability of a transition from R to R' . The rejection and acceptance probabilities are given by,

$$P_{\text{rej}}(\vec{R}'|\vec{R}) = 1 - P_{\text{acc}}(\vec{R}'|\vec{R}) \quad (2.67)$$

$$P_{\text{acc}}(\vec{R}_f|\vec{R}_i) = \min \left(1, \frac{P_{\text{prop}}(\vec{R}_i|\vec{R}_f)\rho(\vec{R}_f)}{P_{\text{prop}}(\vec{R}_f|\vec{R}_i)\rho(\vec{R}_i)} \right) \quad (2.68)$$

where the $P_{\text{prop}}(\vec{R})$ is proposal probability, that can be chosen for efficient sampling of configuration space.

Following the choice of an appropriate trial wave-function, the many body electronic wave function is optimized by a VMC calculation by minimizing the variational energy E_L and the statistical uncertainty resulting from finite sampling in the Monte Carlo integration.

Large number of Monte Carlo steps are necessary to sample the probability distribution. Because a new point is proposed from the last point at each Monte Carlo step, the steps become correlated. This correlation is taken into account by blocking technique.⁵⁹ Each independent block consists of M_s steps that are correlated. The correlation time needs to be considerably smaller than the number of steps for accurate estimation of statistical errors. Additionally, at each step, a tunable step size determines the magnitude of each proposed step from the previous wave function. If step size is too small, the most of the proposed wave functions are accepted, but the walkers are relatively localized due to finite number of steps. Contrarily, if the step size is too large, the most of the steps are rejected, thus the points in the configuration space cannot effectively sample the correct probability distribution.

Another error source due to the approximate wave-function is called systematic errors. Although the method is guaranteed to find a state with a variational energy less than the initial E_v , the success of the method depends on how close the initial wave-function is to the exact ground state. In this study, we perform calculations for Slater determinants built from tight-binding orbitals and mean-field Hubbard orbitals.

2.5. Diffusion Monte Carlo Method

In Diffusion Monte Carlo (DMC) method, the exact ground-state wave-function is used instead of a trial function,⁵⁹

$$E_0 = \frac{\langle \Psi_0 | \hat{H} | \Psi \rangle}{\langle \Psi_0 | \Psi \rangle} = \frac{\int d\vec{R} \Psi_0(\vec{R}) \Psi(\vec{R}) E_L(\vec{R})}{\int d\vec{R} \Psi_0(\vec{R}) \Psi(\vec{R})}, \quad E_L = \frac{\hat{H} \Psi(\vec{R})}{\Psi(\vec{R})} \quad (2.69)$$

Evaluation of the exact ground state wave-function is straightforward if we consider

the time evolution of the wave-function in imaginary time formulation ($t \rightarrow -\frac{i}{\hbar}t$),

$$\Psi(\vec{R}, t) = \sum_n \exp(-(E_n - E_T)t) \Psi_n(\vec{R}) \Psi_n^*(\vec{R}) \Psi(\vec{R}) \quad (2.70)$$

where E_T is the trial energy that is tuned at each step along with the evolution of the wave function. As $t \rightarrow \infty$, the exponential factor decays faster for the states other than the ground-state and the trial energy,

$$\lim_{t \rightarrow \infty} \Psi(\vec{R}, t) = \exp(-(E_0 - E_T)t) \Psi_0(\vec{R}) \Psi_0^*(\vec{R}) \Psi(\vec{R}) \quad (2.71)$$

Time-evolution is evaluated by using an imaginary time propagator so-called Green function $G(\vec{R}_f | \vec{R}_i; t)$,

$$\Psi(\vec{R}_f, t + \tau) = \int d\vec{R} G(\vec{R}_f | \vec{R}; \tau) \Psi(\vec{R}, t) \quad (2.72)$$

$$\begin{aligned} G(\vec{R}_f | \vec{R}_i; \tau) &= \langle \vec{R}_f | \exp(-(\hat{H} - E_T)\tau) | \vec{R}_i \rangle \\ &= \langle \vec{R}_f | \left(\sum_n |\Psi_n\rangle \langle \Psi_n| \exp(-(\hat{H} - E_T)\tau) |\Psi_n\rangle \langle \Psi_n| \right) | \vec{R}_i \rangle \\ &= \sum_n \exp(-(E_n - E_T)\tau) \Psi_n^*(\vec{R}_f) \Psi_n(\vec{R}_i) \end{aligned} \quad (2.73)$$

Importance sampling Green function $\tilde{G}(\vec{R}_f | \vec{R}_i; \tau)$ and mixed distribution $f(\vec{R}, t)$ is defined as,

$$\tilde{G}(\vec{R}_f | \vec{R}_i; \tau) = \Psi(\vec{R}_f) G(\vec{R}_f | \vec{R}_i; \tau) \frac{1}{\Psi(\vec{R}_i)} \quad (2.74)$$

$$f(\vec{R}, t) = \int d\vec{R}_i \tilde{G}(\vec{R}_f | \vec{R}_i; \tau) \Psi^2(\vec{R}_i) \quad (2.75)$$

In the long time limit, the mixed distribution $f(\vec{R}, t)$ becomes proportional to the target distribution, i.e. $f(\vec{R}, t) \propto \Psi_0(\vec{R}) \Psi(\vec{R})$. Because $\tilde{G}(\vec{R}_f | \vec{R}_i; \tau)$ is not a normalized probability distribution, it can be sampled from a weighted distribution,

$$f(\vec{R}, t) = \frac{1}{M} \sum_{k=1}^M \sum_{\alpha=1}^{M_k} w_{k,\alpha} \delta(\vec{R} - \vec{R}_{k,\alpha}) \quad (2.76)$$

where M is the number of Monte Carlo steps and M_k is the population of walkers that

change during branching birth and death process. This process improves sampling efficiency by adjusting the walker population and weights in favor of energy minimization and similar-weighted population. The local energy is given by,

$$E_L = \frac{\sum_{k=1}^M \sum_{\alpha=1}^{M_k} w_{k,\alpha} E_L(\vec{R}_{k\alpha})}{\sum_{k=1}^M \sum_{\alpha=1}^{M_k} w_{k,\alpha}} \quad (2.77)$$

In anti-symmetric wave functions, the sign of the wave function changes if two particles are exchanged. An anti-symmetric trial wave function may cause vanishing final distribution if the final wave function is bosonic, i.e. it does not change sign when two particles are exchanged. This is caused by both positive and negative contributions to the weights. To fix this so-called fermionic sign problem, fixed-node approximation is used. In this method, the walkers are not allowed to cross nodes of the wave function. This ensures the fixed sign, however the resulting wave function has the same nodal structure as that of the trial wave function. Since the resulting fixed-node wave function does not necessarily be the correct ground state, the error due to fixed-node wave function is called fixed-node error.

Additionally there are two other types of errors: finite time step error due to finite time propagation and population control error. Finite time step error is the type of the error similar to the step size in VMC calculations, in a way that it is used to tune sample efficiency. The population control error is related to the estimated ground state energy which is used to tune trial energy at each step. This error decreases by increasing the number of walkers.⁵⁹

The spin and charge density operators in DMC method do not commute with the Hamiltonian.⁵⁸ However, there are first order approximations called extrapolated estimators given by,

$$\langle \hat{O} \rangle = 2 \langle \hat{O} \rangle_{\text{DMC}} - \langle \hat{O} \rangle_{\text{VMC}} + \mathcal{O} \left((\Psi_d - \Psi_v)^2 \right) \quad (2.78)$$

$$\langle \hat{O} \rangle = \langle \hat{O} \rangle_{\text{DMC}}^2 \langle \hat{O} \rangle_{\text{VMC}}^{-1} + \mathcal{O} \left((\Psi_d - \Psi_v)^2 \right) \quad (2.79)$$

where Ψ_d and Ψ_v are DMC and VMC wave functions respectively.

CHAPTER 3

RESULTS

3.1. 16-site Rhombohedral Lattice

In this part, we performed VMC and DMC calculations for 4x4 rhombohedral cell of triangular lattice based on MFH and TB determinants. In MFH calculations, we start with single orbital tight-binding Hamiltonian given by,

$$\hat{H}_{\text{TB}} = \sum_{\langle i,j \rangle, \sigma} t_{ij} \left(\hat{c}_{i\sigma}^\dagger \hat{c}_{j\sigma} + \hat{c}_{j\sigma}^\dagger \hat{c}_{i\sigma} \right) \quad (3.1)$$

where t_{ij} are the hopping amplitudes between sites i and j given by $t_{ij} = \delta_{|r_i - r_j|, a}$ with lattice constant a , i.e. only the nearest neighbor interactions are considered. Figure 3.1 shows the lattice and couplings for this model. In our calculations, the value of t_{ij} is set to one, since the orbital coefficients do not depend on the scale of the hopping parameters.

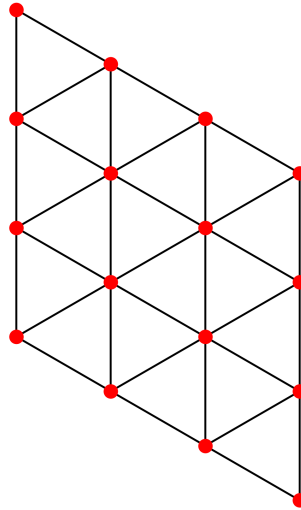


Figure 3.1. 4x4 triangular lattice used used in TB and MFH calculations are shown. Lattice points are shown by red circles while the couplings between the nearest neighbor sites are shown by black lines.

MFH calculations are performed by using eq. 2.56 by utilizing algorithms 2.1 and 2.2 for varied filling factors. The filling factor is defined by,

$$\nu = N_{\text{elec}}/N_{\text{orb}} \quad (3.2)$$

where N_{elec} and N_{orb} are the number of electrons and orbitals respectively. In our case, each site correspond to one localized orbital, therefore $N_{\text{orb}} = N_c$ where N_c is the number of centers. Since each orbital can occupy at most 2 electrons, ν can take values between 0 and 2. To find the ground state for any ν , we perform a scan over possible values of the z -component of spin, i.e. S_z values. S_z is defined by,

$$S_z = \frac{N_{\uparrow} - N_{\downarrow}}{2} \quad (3.3)$$

where $N_{\uparrow}(N_{\downarrow})$ is the number of spin- \uparrow and spin- \downarrow electrons, which add up to the total number of electrons $N_{\text{elec}} = N_{\uparrow} + N_{\downarrow}$.

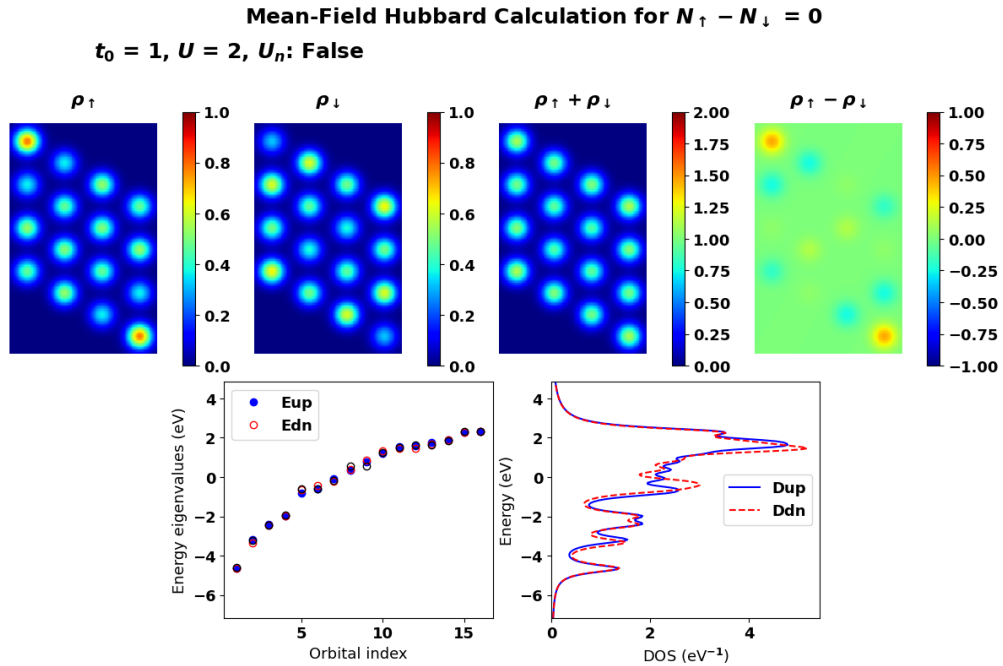


Figure 3.2. Spin densities, charge densities, energy spectrum and DOS of MFH ground state ($S_z = 0$) of 4x4 rhombohedral lattice is shown. Red and blue colors correspond to down and up orbitals in energy and DOS figures. The interaction strength is $\kappa U/t = 2$, where κ is relative dielectric constant.

The minimum and maximum number of S_z are determined by the total number of electrons,

$$S_z^{\max} = M/2 \quad (3.4)$$

$$S_z^{\min} = \text{mod}(M, 2)/2 \quad (3.5)$$

$$M = \min(N_{\text{elec}}, 2N_{\text{orb}} - N_{\text{elec}}) \quad (3.6)$$

where M ensures that each orbital is occupied by one spin- \uparrow electrons at most. If the total number of electrons is odd (even), the minimum possible S_z value is $1/2$ (0). For half-filled ($\nu = 1/2$) orbitals of 4×4 rhombohedral lattice, the MFH ground state spin is found to be $S_z = 0$. The ground state spin and charge densities for this system are shown in figure 3.2. Densities are visualized by multiplying the probability densities $|\psi_n|^2$ of each site n by gaussians of uniform width.

By using the Slater determinant built from TB orbitals and MFH ground state spin- \uparrow and spin- \downarrow orbitals for filling factors $\nu \in [0, 8]$, VMC calculations were performed. In VMC calculations, the finite Moiré potential shown in Figure 2.3 is fitted to moiré potential parameters from literature.³² The lattice constant is $a = 7.5$ nm, twist angle $\theta = 0^\circ$, moiré potential amplitude is $V_m = 6.3$ meV, moiré potential phase is $\psi = 0^\circ$. Effective mass of electrons is given by $m_r = 0.7$ with $m_r = m_{\text{eff}}/m_e$, where m_e is the electron mass.³² Relative dielectric coefficient κ is chosen to be 20. Effective atomic units are used in our calculations. The conversion formula from nanometers and electron-volts to effective Hartree atomic units are given by,

$$\begin{aligned} L_{\text{a.u.}} &= \left(a_0 \frac{\kappa}{m_r} \right)^{-1} L_{\text{nm}} \quad (3.7) \\ &= 0.6614041436227691 L_{\text{nm}} \end{aligned}$$

$$\begin{aligned} E_{\text{a.u.}} &= \left(E_{\text{H}} \frac{m_r}{\kappa^2} \right)^{-1} E_{\text{eV}} \quad (3.8) \\ &= 20.99961267180285 E_{\text{eV}} \end{aligned}$$

where Bohr radius $a_0 = 0.05291772109$ nm and Hartree energy $E_{\text{H}} = 27.21138624598$ eV. The resulting acceptance ratios, energy values and Root Mean Square (RMS) errors are given by table 3.1. In these calculations, a scan over step sizes was performed to maintain an acceptance rate around 0.5. Table 3.1 shows that the minimum energy for

both trial wave functions occurs at $S_z = 2$. However, for TB trial wave function, the energy difference between $S_z = 2$ and $S_z = 4$ is about RMS errors of their energies, the possibility of the ground state at $S_z = 4$ cannot be ignored. Additionally, to determine the ground state S_z more accurately, a DMC calculation by using the optimized VMC wave function is required.

Table 3.1. Acceptance rates, total energies, and RMS errors in total energies of VMC calculations performed by by using TB and MFH trial wave functions.

Sz	TB Trial WF			MFH Trial WF		
	Acceptance	Energy (meV)	RMS Error (meV)	Acceptance	Energy (meV)	RMS Error (meV)
0	0.4511	-1144.165	0.0239	0.4507	-1144.7771	0.026
1	0.4549	-1144.9694	0.0247	0.4544	-1145.072	0.0245
2	0.4513	-1145.0975	0.0239	0.4534	-1145.4317	0.0239
3	0.55	-1144.5201	0.0234	0.5501	-1143.1239	0.0226
4	0.5403	-1145.0783	0.0231	0.5407	-1141.8551	0.0237
5	0.5299	-1141.9651	0.023	0.5295	-1142.3413	0.022
6	0.5216	-1144.8749	0.0217	0.5217	-1144.8021	0.0216
7	0.5037	-1141.9228	0.0223	0.5058	-1143.3276	0.021
8	0.4861	-1145.0915	0.0196	0.4862	-1145.0878	0.0204

Table 3.2. Acceptance rates, ratios of correlation times to number of steps, total energies, RMS errors in total energies and populaton control errors of DMC calculations performed by using VMC-optimized TB trial wave functions for $\nu = 1$ in 4x4 rhombohedral lattice.

Sz	TB Trial WF				
	Acceptance	Tcor/Nstep	Energy (meV)	RMS Error (meV)	Pop. Cont. Error (meV)
0	0.9977	0.2061	-1185.8588	0.0873	0.1778
1	0.9977	0.1833	-1186.2149	0.0809	0.1573
2	0.9977	0.1922	-1185.3229	0.0818	0.1564
3	0.9977	0.1646	-1184.5765	0.0739	0.1493
4	0.9977	0.185	-1183.7343	0.0765	0.1425
5	0.9976	0.2421	-1181.3833	0.0907	0.1871
6	0.9976	0.243	-1180.8045	0.0857	0.1618
7	0.9975	0.2	-1175.3443	0.0739	0.1347
8	0.9975	0.2358	-1171.4014	0.0799	0.1485

Tables 3.2 and 3.3 show the results of DMC calculations by using VMC-optimized TB and MFH trial wavefunctions respectively. The ground state S_z is 1 for both TB and MFH trial wave functions with similar energies. Because the population control error is considerably larger than the RMS error, the former is taken to be the main error in our

calculations. The population control error is reduced by increased number of walkers or reduced time step. Lowering time step causes high correlation time, therefore one needs to increase the number of steps which leads to higher computation time. Because reducing correlation time increases computation time, the ratio of correlation time to number of steps is kept around 20%.

VMC and extrapolated DMC spin and charge densities determined from TB trial wave function of ground state spin ($S_z = 1$) is shown in figures 3.3a and 3.3c. The figure shows that DMC densities show triangularly symmetric distribution around lattice sites where potential wells exist, unlike VMC densities that have spherically symmetric charge distributions around lattice sites. Because kinetic energies of the electrons are relatively high, they gather around the edge sites, and uniformly distributed around inner sites, indicating metallic behavior. Extrapolated DMC densities for VMC-optimized TB and MFH trial wave functions are similar, in agreement with the energies given by tables 3.2 and 3.3.

Table 3.3. Acceptance rates, ratios of correlation times to number of steps, total energies, RMS errors in total energies and populaton control errors of DMC calculations performed by using VMC-optimized MFH trial wave functions for $\nu = 1$ in 4x4 rhombohedral lattice.

Sz	MFH Trial WF				
	Acceptance	Tcor/Nstep	Energy (meV)	RMS Error (meV)	Pop. Cont. Error (meV)
0	0.9977	0.1971	-1185.4647	0.0824	0.1597
1	0.9978	0.1689	-1186.2252	0.0775	0.1657
2	0.9978	0.1972	-1185.2975	0.0831	0.1631
3	0.9977	0.199	-1184.063	0.081	0.1574
4	0.9977	0.224	-1182.2563	0.0895	0.1753
5	0.9976	0.2297	-1181.5547	0.0866	0.1693
6	0.9976	0.2637	-1181.0201	0.0918	0.1759
7	0.9976	0.2175	-1176.8035	0.0773	0.1432
8	0.9975	0.2017	-1171.5068	0.0741	0.1443

Table 3.4. For 4x4 rhombohedral lattice, 8 e^- ($\nu = 1/2$) VMC acceptance, energies and RMS errors for each S_z . The lowest energy trial wavefunctions are shown.

Sz	Trial WF	Acceptance	Energy (meV)	RMS Error (meV)
0	MFH	0.516	-792.7676	0.0166
1	MFH	0.5138	-792.7513	0.0157
2	TB	0.5133	-791.2036	0.016
3	MFH	0.4919	-791.4444	0.0159
4	TB	0.4895	-790.31	0.0162

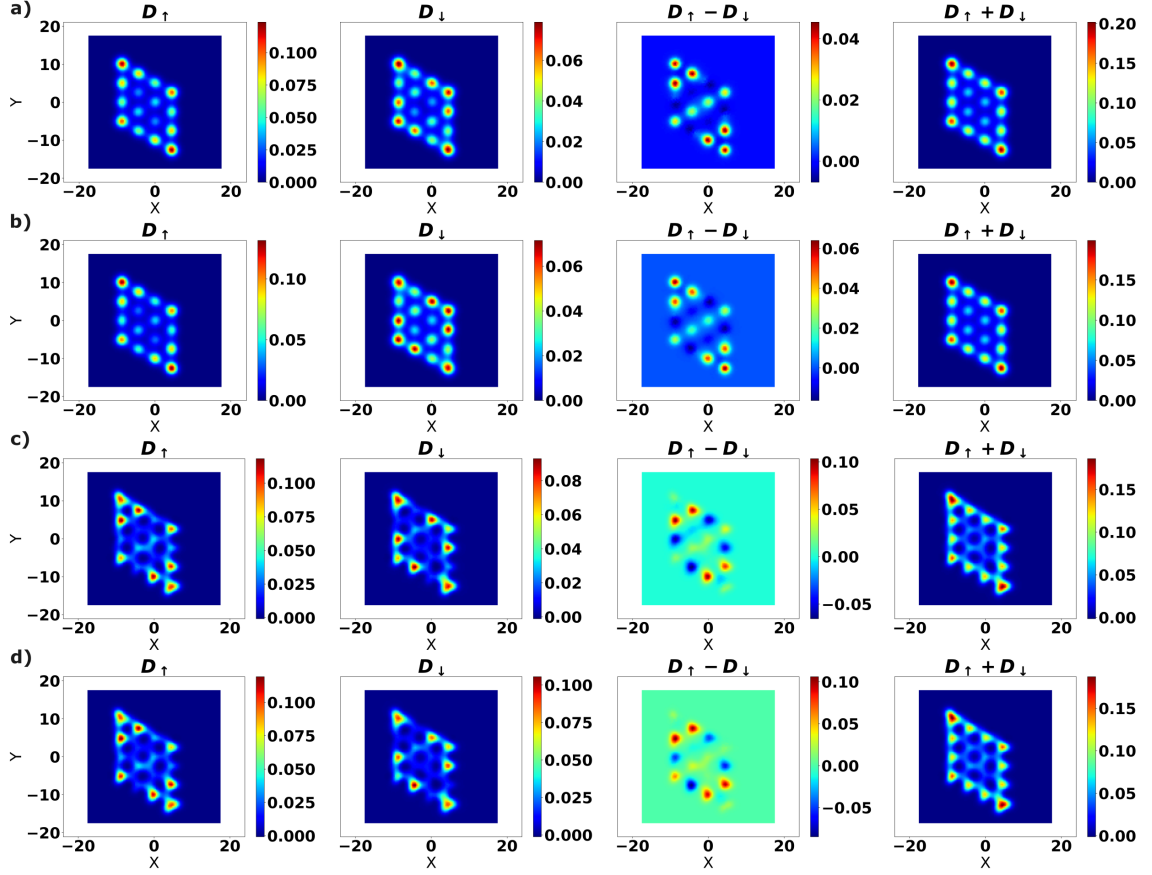


Figure 3.3. For 4×4 rhombohedral lattice, ground state ($S_z = 1$) spin- \uparrow - spin- \downarrow densities (column 1-2), spin densities (column 3) and charge densities (column 4) for (a) VMC with TB trial w.f., (b) VMC with MFH trial w.f., (c) DMC with VMC-optimized TB trial w.f., (d) DMC with VMC-optimized MFH trial w.f. are shown. Density plots for DMC calculations in (c) and (d) are extrapolated by using equation 2.78.

Similarly, for $\nu = 1/2$ and $\nu = 3/2$, VMC results are shown in table 3.4 and table 3.5, DMC results are shown in table 3.6 and table 3.7. For $\nu = 1/2$ both VMC and DMC results show that the ground state S_z is zero, i.e. the system is not magnetic. However, for $\nu = 3/2$ both VMC and DMC results indicate the ground state is at $S_z = 2$, i.e. the system is ferromagnetic. Figure 3.4 shows extrapolated ground state spin and charge densities for $\nu = 1/2, 1, 3/2$. As the number of electrons increase, the number of spin- \uparrow electrons increase. Due to exchange interaction between spin- \uparrow electrons, they try to avoid each other, leading to a more uniform distribution throughout the system. However, because the number of spin- \downarrow electrons are relatively low, they prefer edge sites. Based on the ground state S_z values obtained from DMC calculations by using VMC-optimized

wave functions for three filling factors, we conclude that a paramagnetic-ferromagnetic phase transition occur between $\nu = 1$ and $\nu = 3/2$, in agreement with recent experimental study by Ciorciaro et. al.³² Because the ferromagnetic phase is expected to be stronger for $\nu = 3/2$ than that for $\nu = 1$ theoretically,³³ DMC calculations were performed for filling factors between $\nu = 1$ and $\nu = 3/2$ to verify this behavior. Since the difference in ground state energies of different trial wave functions are not significant, TB trial wave functions are used for these calculations.

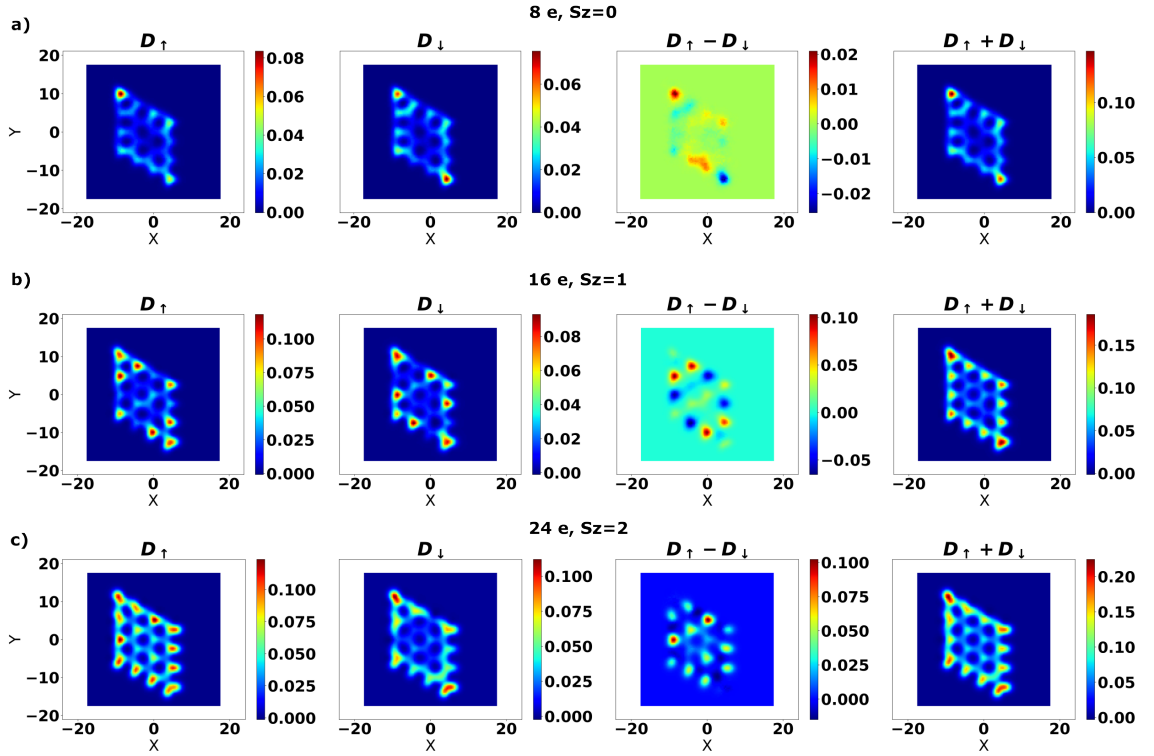


Figure 3.4. For 4x4 rhombohedral lattice, ground state extrapolated spin- \uparrow - spin- \downarrow densities (column 1-2), extrapolated spin densities (column 3) and extrapolated charge densities (column 4) for (a) $\nu = 1/2$, (b) $\nu = 1$ and (c) $\nu = 3/2$.

Table 3.5. For 4x4 rhombohedral lattice, 24 e⁻ ($\nu = 3/2$) VMC acceptance, energies and RMS errors for each S_z . The lowest energy trial wavefunctions are shown.

S_z	Trial WF	Acceptance	Energy (meV)	RMS Error (meV)
0	TB	0.5552	-1049.9745	0.0278
1	TB	0.5522	-1049.6498	0.0294
2	TB	0.5496	-1052.1763	0.0288
3	TB	0.5425	-1050.1342	0.0297
4	TB	0.544	-1045.3491	0.0303

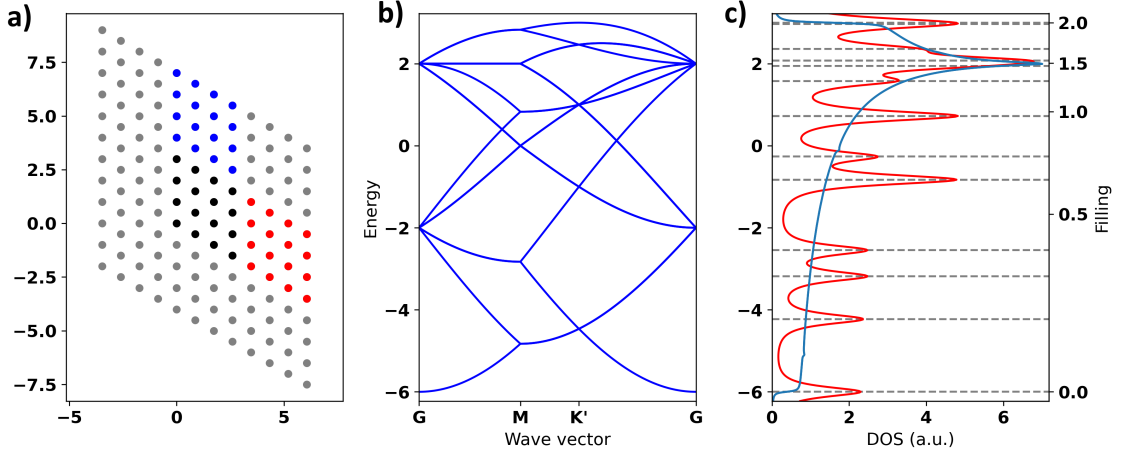


Figure 3.5. For (a) 4x4 rhombohedral unit cell sites are shown by black dots, unit cells translated by \vec{a}_1 and \vec{a}_2 vectors are shown by blue and red dots. (b) Band structure obtained by using first nearest-neighbor TB model with hopping parameter $t = 1$ for aforementioned unit cell. (c) DOS obtained by equation 2.26 is shown. Blue lines and red lines correspond to DOS of periodic and finite lattices respectively. Discrete energy levels of finite system are depicted by horizontal dashed lines. Left and right y-axes correspond to energy E and filling factor ν respectively. Van Hove singularity occurs at $E = 2t$ or $\nu = 3/2$.

Table 3.6. For 4x4 rhombohedral lattice, $8 e^-$ ($\nu = 1/2$) DMC acceptance, correlation time-number of steps ratio, energies, RMS errors and population control errors for each S_z . The lowest energy trial wavefunctions are shown.

Sz	Trial WF	Acceptance	Tcor/Nstep	Energy (meV)	RMS Error (meV)	Pop. Cont. Error (meV)
0	TB	0.9982	0.1335	-811.1124	0.0835	0.1547
1	TB	0.9981	0.1301	-810.8835	0.083	0.1641
2	TB	0.9982	0.1413	-809.8932	0.0862	0.1638
3	TB	0.9981	0.1373	-809.0669	0.0835	0.1627
4	MFH	0.998	0.1478	-807.0954	0.0869	0.181

Van Hove singularity around $\nu \approx 3/2$ (see Figure 1.5a) show degenerate orbitals that can trigger itinerant ferromagnetism. The singularity in DOS can easily be seen in Figure 3.5c obtained by the nearest neighbor TB model of periodic triangular lattice shown in Figure 3.5a. Note that DOS of finite 4x4 has multiple peaks due to finite number of discrete energy levels instead of continuous bands. We performed an analysis to explore itinerant ferromagnetism based on TB spectrum based on the fact that the electrons occu-

pying different states in a narrow energy window will most likely occupy the same spin due to exchange interactions. Because odd (even) number electrons lead to $S_z^{\min} = 1/2$ ($S_z^{\min} = 0$), the expected S_z values for non-degenerate orbitals alternate with respect to the number of electrons. We compared the expected ground state S_z based on TB spectrum and DMC results for varied number of electrons between 0 and 3/2. For 4x4 rhombohedral lattice TB spectrum, expected S_z and S_z determined by DMC calculations for various number of electrons are shown in Figure 3.6a. Ground state S_z values are taken to be the maximum S_z within the error bar of minimum energy values. For 25 electrons, $S_z = 1/2$ and $S_z = 3/2$ lie within an error bar, thus $S_z = 3/2$ is taken as reference value. Similarly, for 28 electrons, $S_z = 0$ and $S_z = 2$ lie within an error bar, therefore $S_z = 2$ is taken as the reference value. Around 3/2-filling, determined S_z values are generally higher than the expected values, indicating strong itinerant ferromagnetism. As an example, the orbital occupation for 24 electrons is visualized in Figure 3.6b, where the ground state S_z value is 2, the number of spin- \uparrow electrons is $N_\uparrow = 14$ and the number of spin- \downarrow electrons is $N_\downarrow = 10$. The first ten orbitals are occupied by both spin-up and spin-down electrons and the remaining four spin- \uparrow electrons occupy the next four orbitals.

Table 3.7. For 4x4 rhombohedral lattice, 24 e^- ($\nu = 3/2$) DMC acceptance, correlation time-number of steps ratio, energies, RMS errors and population control errors for each S_z . The lowest energy trial wavefunctions are shown.

S_z	Trial WF	Acceptance	Tcor/Nstep	Energy (meV)	RMS Error (meV)	Pop. Cont. Error (meV)
0	TB	0.9934	0.2588	-1124.5261	0.0998	0.2136
1	TB	0.9933	0.2219	-1124.7641	0.0909	0.1992
2	TB	0.9934	0.2346	-1125.6276	0.0904	0.1955
3	TB	0.9933	0.2326	-1123.7667	0.0888	0.1935
4	TB	0.9933	0.2676	-1121.2114	0.106	0.2627

3.2. 19-site Radial Lattice With Guiding Potential

The electrons in our system have large kinetic energy and strong correlation which causes electrons gather at the edges, unlike those in periodic systems. To that end, we introduced a Gaussian-type guiding potential which reduces kinetic energies of the electrons, therefore improving uniformity of the charge density. Because Gaussian potential has radial symmetry, we use a radially symmetric 19-site lattice shown in Figure 3.7. Af-

ter trial and error, we determined a suitable guiding Gaussian with amplitude V_g is large enough to be at the order of moiré potential ($-28V_m$). The width ρ_g is at the order of the size of the lattice, and stiffness s_g is 0.8. The potential and guiding Gaussian for this system are shown in Figures 3.8b and 3.8c respectively.

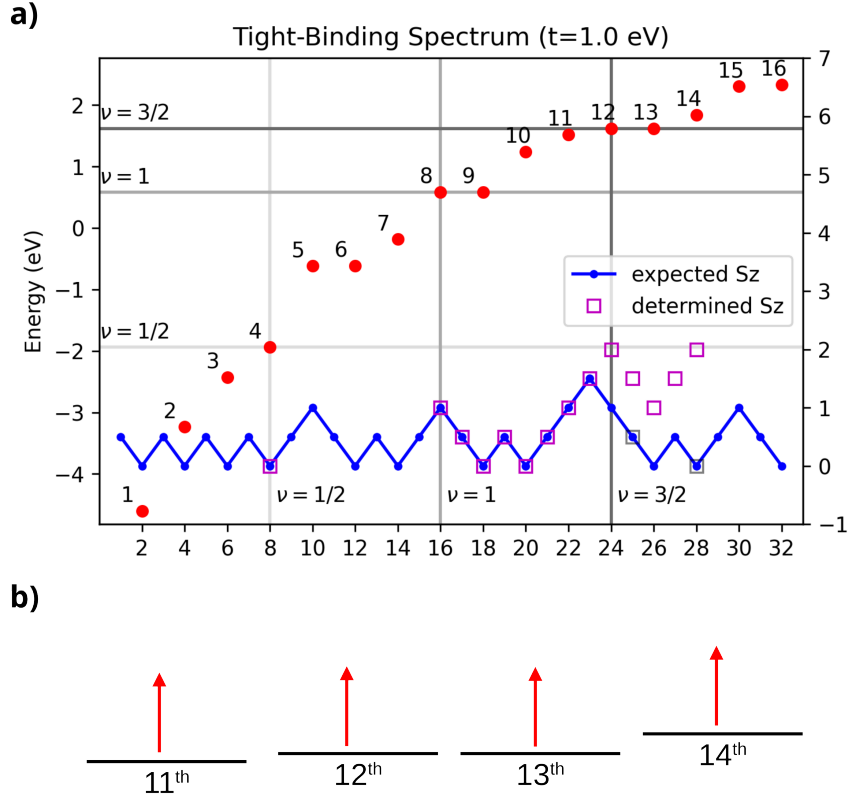


Figure 3.6. (a) TB spectrum for 4x4 rhombohedral lattice (red circles). Blue dotted lines correspond to the expected S_z values for expected spin values due to degeneracies in TB spectrum. Magenta squares correspond to the ground state S_z values obtained from DMC calculations. Some of the calculations resulted in multiple S_z values within an error bar around minimum energy. Lower S_z values are shown by gray squares. (b) Orbital occupation of singly occupied orbitals for 24 electrons.

Spin and charge densities for $\nu \approx 0.5$, $\nu = 1$ and $\nu \approx 1.5$ are shown in Figure 3.9. The guiding potential is chosen to provide nearly uniform charge density at half filling (see Figure 3.9b). Because of a deep gaussian well centered at the origin, the electrons occupy a narrow circular area at the center at low filling values as shown for $\nu \approx 0.5$ in Figure 3.9a. As the number of electrons increase, spin ordering of electrons become apparent where

abundant spin- \uparrow electrons occupy the wells and spin- \downarrow electrons are distributed in between (see Figure 3.9c). This behavior agrees with the findings of the study by Ciorciaro et. al.³² where antiferromagnetic spin susceptibility is observed for $\nu > 3/2$, as shown in Figure 1.5b.

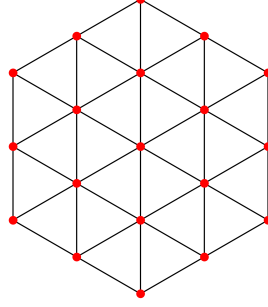


Figure 3.7. 19-site radial lattice used in tight-binding and mean-field Hubbard calculations are shown. Lattice points are shown by red circles while the couplings between the nearest neighbor sites are shown by black lines.

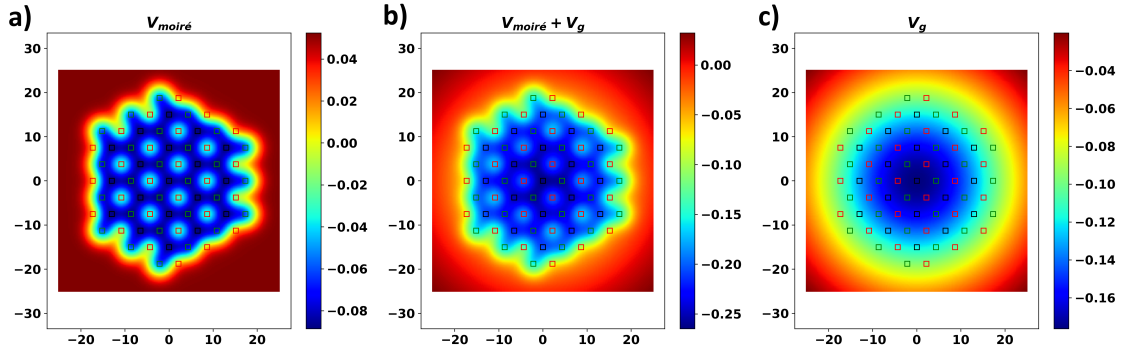


Figure 3.8. (a) Moiré potential, (b) Moiré potential with guiding potential and (c) guiding potential for radial 19-site lattice in eV. Black, red and green squares correspond to potential wells, hills and midpoints respectively. Guiding gaussian amplitude $V_g = -28V_m = -176.4$ meV, stiffness $s_g = 0.8$ and width ρ_g is at the order of the size of the lattice.

For 19-site radial lattice, we performed an analysis similar to that for 16-site rhombohedral lattice shown in Figure 3.6a. We performed DMC calculations by using both TB trial wave functions and MFH trial wave functions with $\kappa U/t = 2.5$. The expected and determined S_z values are shown in Figure 3.10a. In general, DMC results agree with the

expected spin values determined from the analysis on TB spectrum. For 23, 24 and 28 electrons, we determined multiple S_z values within an error bar around minimum energy, therefore the maximum S_z values were chosen as reference. Although calculations for some spin values failed to converge for more than 28 electrons, by comparing energies of TB and MFH trial wave functions we deduced that the ground state S_z values are likely those shown in Figure 3.10a.

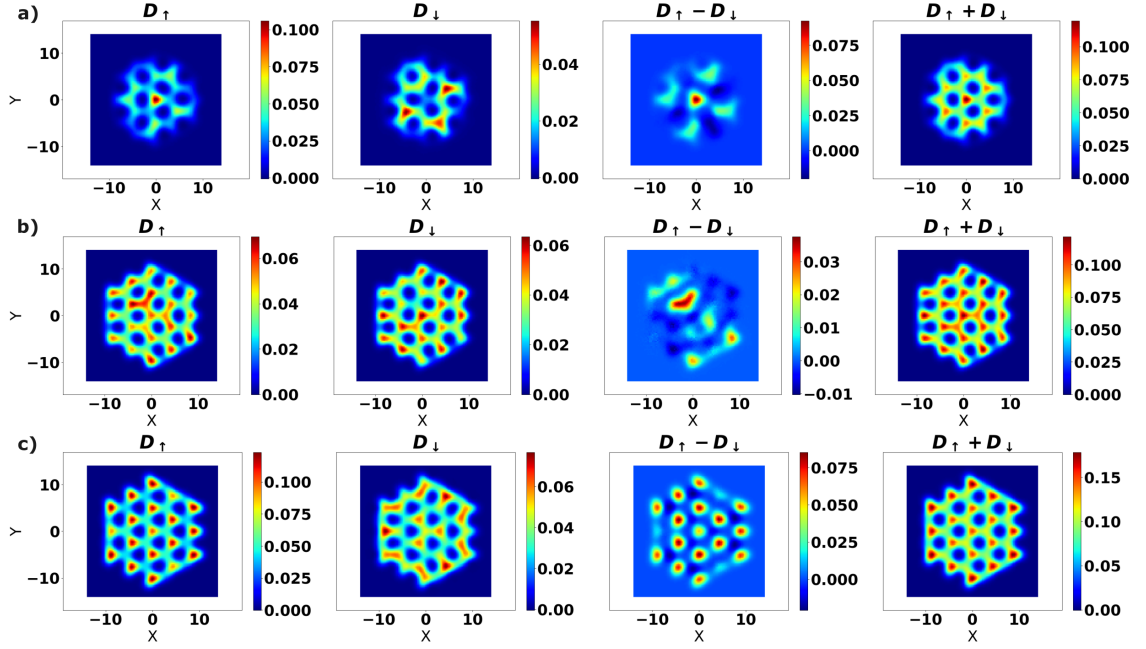


Figure 3.9. Ground state spin and charge densities obtained by DMC calculations by using VMC-optimized TB trial wave functions for (a) 10 electrons ($\nu = 10/19 = 0.5263$, $S_z = 1$), (b) 19 electrons ($\nu = 1$, $S_z = 1/2$), (c) 30 electrons ($\nu = 30/19 = 1.579$, $S_z = 3$).

3.3. Wigner Crystals

DMC calculations in previous sections indicate large kinetic energy from charge density plots in which the electrons tend to build up at the edge sites. To explore Wigner crystal states, we reduced kinetic energy by increasing Moiré potential amplitude V_m from 6.3 meV to 25 meV. Guiding potential at low densities dominates over Coulomb repulsion, gluing electrons together around the central site. Therefore, guiding potential is not used in this part. Other simulation parameters are the same as the previous sections. Because TB trial wave functions give lower energies with respect to MFH trial wave functions, TB

trial wave functions are used for the calculations in this part. For 7 electrons ($\nu = 7/19 = 0.3684 \approx 1/3$), spin energies are given by Table 3.8. The lowest energy S_z values are $1/2$ and $3/2$ but the energies cannot be distinguishable due to large population control error.

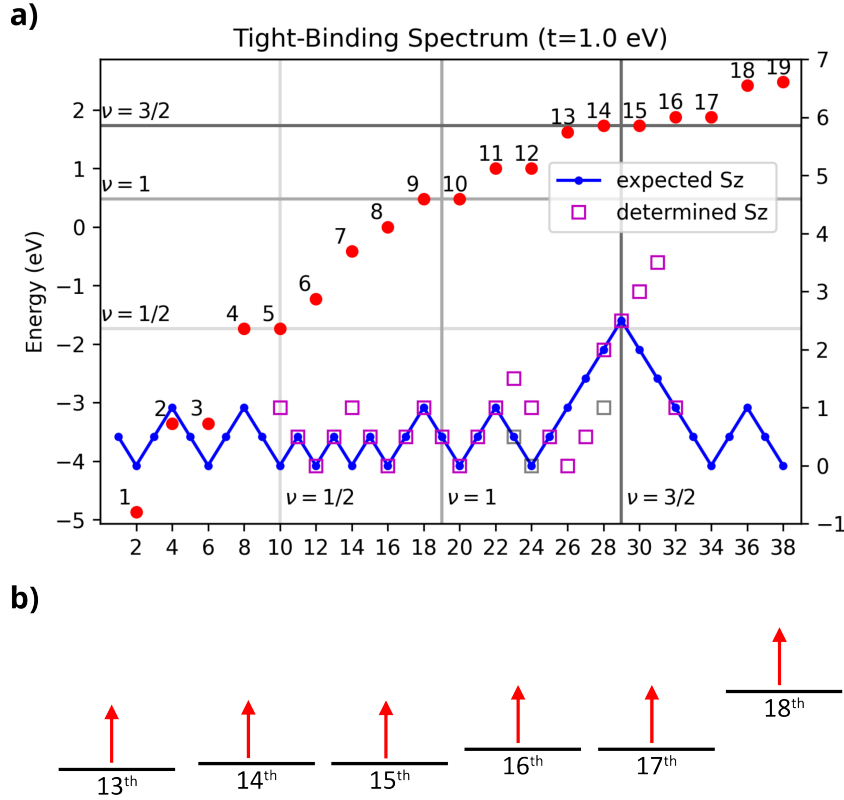


Figure 3.10. (a) TB spectrum for 19-site radial lattice (red circles). Blue dotted lines correspond to the expected S_z values for expected spin values due to degeneracies in TB spectrum. Magenta squares correspond to the ground state S_z values obtained from DMC calculations. Some of the calculations resulted in multiple S_z values within an error bar around minimum energy. Lower S_z values are shown by gray squares. (b) Orbital occupation of singly occupied orbitals for 30 electrons.

Table 3.8. S_z , energy, RMS error in energy and population control error for 7 electrons in 19-site radial lattice with $V_m = 25$ meV.

S_z	Energy (meV)	RMS Error (meV)	Pop. Cont. Error (meV)
1/2	-3471.4012	0.7475	2.1021
3/2	-3470.6498	0.6097	0.8538
5/2	-3462.62874	0.8302	1.9981
7/2	-3466.70186	0.8843	2.4142

Extrapolated charge densities for $S_z \in [7/2, 1/2]$ are shown in Figures 3.11a-d in descending order. The crystalline behavior is observed for maximum polarization ($S_z = 7/2$). For $S_z = 7/2$, the distance between sites are the largest and equal to each other, indicating that the Coulomb repulsion between electrons tries to maximize the distance between them to minimize the energy. As S_z decreases, i.e. number of spin- \downarrow electrons increases, the distance between electrons decreases, and the configuration becomes less crystalline, more uniform at the edges. This behavior can be explained by exchange interaction between the electrons of the same spin. The first two columns of Figures 3.13a-d show the densities for spin- \uparrow and spin- \downarrow electrons respectively. As the number of spin- \uparrow (spin- \downarrow) electrons decreases (increases), the distance between the electrons in the same shell decreases due to reduced exchange interaction. Because correlation strength does not change, the electrons are distributed over edge sites. The reason that the lowest energy state is for $S_z = 1/2$ is most likely due to the reduced exchange energy.

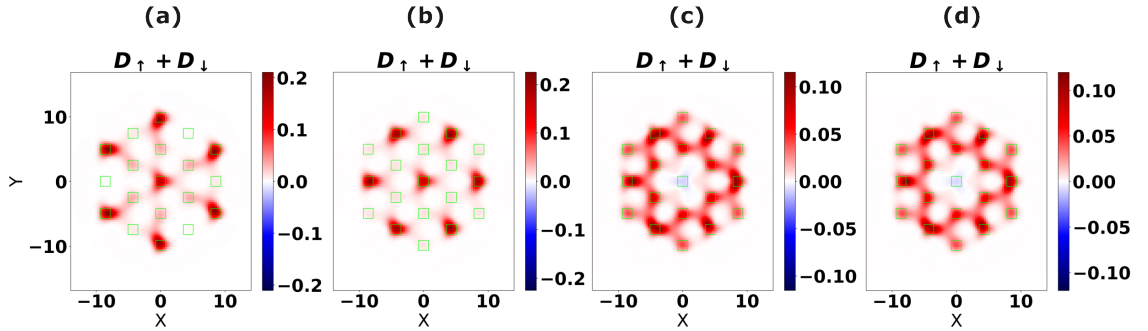


Figure 3.11. Extrapolated charge densities for (a) $S_z = 7/2$, (b) $S_z = 5/2$, (c) $S_z = 3/2$ and (d) $S_z = 1/2$.

For minimal polarization ($S_z = 1/2$), spin- \uparrow and spin- \downarrow electrons are localized in different sites as seen in Figure 3.13a. For better understanding of spin ordering, pair densities were determined by fixing a spin- \uparrow electron to a site with high spin- \uparrow electron density. We denote the pair densities with two subscripts D_{ij} where i is the spin of the fixed electron and j is the other spin of the pair. The difference $D_{\uparrow\uparrow} - D_{\uparrow\downarrow}$ has positive (negative) values around the sites that are occupied by spin- \uparrow (spin- \downarrow) electrons with respect to the fixed spin- \uparrow electron. Figure 3.12a shows $D_{\uparrow\uparrow} - D_{\uparrow\downarrow}$ for $S_z = 1/2$ which shows antiferromagnetic ordering. However, the antiferromagnetic ordering vanishes for $S_z = 3/2$ (see Figure 3.12b), due to spin- \uparrow and spin- \downarrow electrons occupying the same sites

as seen in Figure 3.13b.

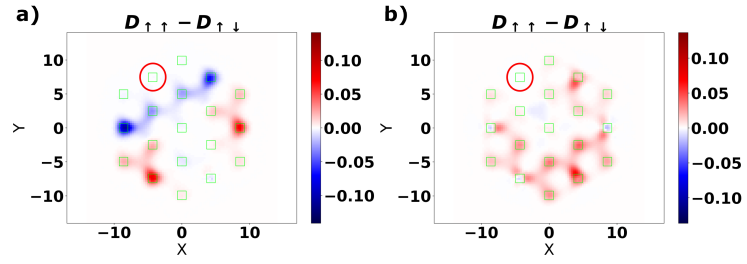


Figure 3.12. Extrapolated pair polarization $D_{\uparrow\uparrow} - D_{\uparrow\downarrow}$ (a) $S_z = 1/2$ and (b) $S_z = 3/2$. The fixed site is shown inside the red circle.

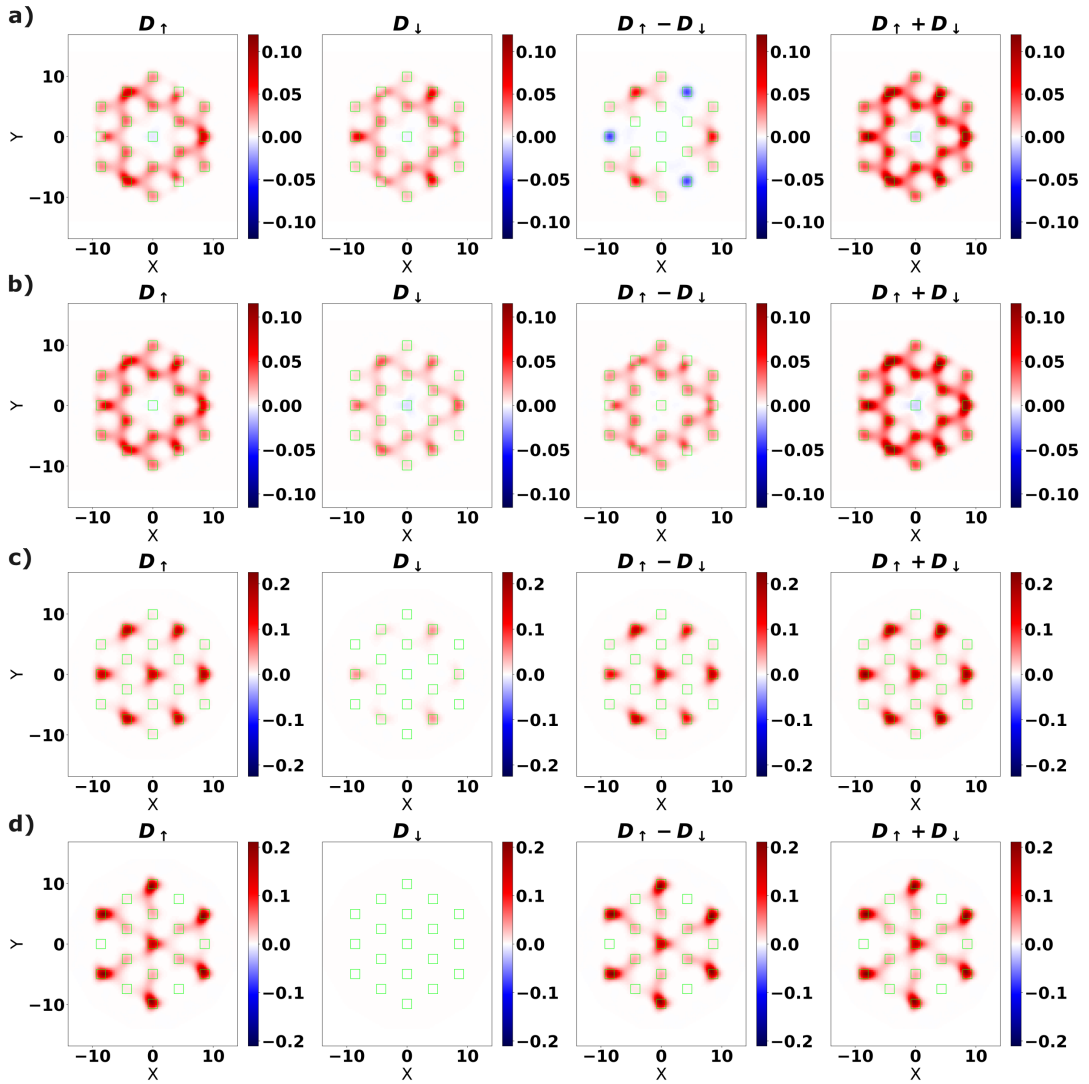


Figure 3.13. Extrapolated spin and charge densities for (a) $S_z = 1/2$, (b) $S_z = 3/2$, (c) $S_z = 5/2$ and (d) $S_z = 7/2$.

CHAPTER 4

CONCLUSION

In this study, we investigate the magnetic phases of finite Moiré heterostructures by using Diffusion and Variational Monte Carlo methods with tight-binding and mean-field Hubbard trial wave functions. The methodology is applicable to other moiré heterobilayers with the change of moiré potential parameters (V_m, ϕ), lattice constant a , relative effective carrier mass m_r and relative dielectric constant κ . Tunability of V_m by pressure and κ by electric field strength introduce additional degrees of freedom to be investigated. However, they are not considered in the current scope of this study, leaving room for future work.

So far, there is only one available DMC study known to us on moiré heterostructures by Yang et. al.⁶¹ This study on periodic moiré heterostructures investigates phase transitions at half-filling between paramagnetic, ferromagnetic, stripe and 120° Neel ordered magnetic phases with respect to moiré potential and interaction strength by using DFT combined with DMC calculations, in a similar way to the exact diagonalization study by Hu and MacDonald.²⁹ In this work, we focus on itinerant ferromagnetism via electron doping and Wigner crystal at low density in finite systems via DMC calculations. To that end a finite potential is designed to approximate periodic moiré potential inside the lattice and grows to its maximum value outside, confining the charge carriers inside the system.

Finite moiré potentials given by equation 2.2 used in this study are simply sums of Gaussian-like functions that can be used to approximate periodic moiré potentials given by equation 1.1. Any d -dimensional function can be approximated as a sum of d -dimensional Gaussians centered at various points in d -dimensional space. Because we restrict Gaussians to the sublattices with fixed parameters, stiffness (s) parameter introduces another degree of freedom for better approximation. In our case, while the first two Gaussian-like functions used to approximate periodic moiré potential are typical Gaussians, the third one has a negative stiffness as shown in Figure 2.1. This methodology can easily be generalized to approximate any periodic potential for finite systems.

Due to enhanced DOS at $\nu = 3/2$ -filling in both 16-site rhombohedral and 19-site radial geometries, the ground state S_z is enhanced. This behavior agrees with the theoret-

ical study by Potasz et. al.,³³ although the system parameters they use for WSe₂/WS₂ are different than those we use for MoSe₂/WS₂. An experimental study by Ciorciaro et. al.³² shows that temperature dependent magnetic susceptibilities of MoSe₂/WS₂ heterobilayers indicate ferromagnetism for fillings between $\nu = 1$ and $\nu = 3/2$, as shown in Figure 1.5b. Additionally, in the same study the authors state that for fillings $\nu = 1$ and below the system is paramagnetic, and surprisingly ferromagnetic to antiferromagnetic phase transition occurs at $\nu = 3/2$ (see Figure 1.5b).³² In our results, ferromagnetic ground state is obtained around $\nu = 3/2$ as shown by Figure 3.6 for rhombohedral lattice and by Figure 3.10 for radial lattice. The spin densities of 19-site radial geometry for $\nu = 30/19 \approx 3/2$ show magnetic ordering similar to ferrimagnetism with dominant spin- \uparrow contribution (see the third column of Figure 3.9c). This behavior might be related to the unexpected antiferromagnetic behavior in spin susceptibilities around $\nu = 3/2$ obtained by Ciorciaro et. al.³² A larger geometry could reveal the nature of this behavior due to the increased number of orbitals, i.e. an increased number possible filling values.

The spurious spin polarization for $\nu = 0.5$ seen in Figure 1.5a³³ was not observed in our results for 19-site radial geometry except for $\nu = 10/19$ and $\nu = 14/19$ (see Figure 3.10a). In this regime, the charges are pulled towards center due to large guiding Gaussian. For 16-site rhombohedral geometry, the ground state is for $S_z = 0$ at $\nu = 0.5$. Spin ordering was not seen in both geometries at $\nu = 0.5$, therefore consistent with the paramagnetic behavior at lower fillings shown in Figure 1.5b.³²

Wigner crystal at $1/3$ and $2/3$ fillings are expected in WS₂/WSe₂ moiré heterostructures.^{11,31,37} DMC calculations for 7 electrons in 19-site radial geometry ($\nu \approx 1/3$) of MoSe₂/WS₂ heterobilayers were performed by increasing moiré potential amplitude V_m from 6.3 meV to 25 meV. Although Wigner crystal was observed for maximum $S_z = 7/2$ shown in Figure 3.11a, it has higher energy than $S_z = 1/2$ and $S_z = 3/2$ as shown in Table 3.8. The electron configuration for $S_z = 7/2$ is as the expected configuration obtained from classical Monte Carlo simulations of electron gas in parabolic potential, with one electron in the inner shell and six electrons in the outer shell.⁶² Spin densities of $S_z = 1/2$ indicate antiferromagnetic order shown in the third column of Figure 3.13a. Extrapolated pair polarizations verify the aforementioned antiferromagnetism (see Figure 3.12a. Despite that $S_z = 1/2$ and $S_z = 3/2$ states are not distinguishable due to large population control error, it is possible to obtain antiferromagnetic ground state by tuning the potential

and lattice constant (via twist angle). An isolated antiferromagnetic ground state combined with spin-polarized Wigner crystal allows one to switch between two phases via an out-of-plane magnetic field.

Wigner crystallization can be discussed in terms of Wigner-Seitz parameter r_s given by Equation 1.12. Using the simulation parameters given by Ciorciaro et. al.,³² r_s values for radial lattice are calculated as 3.42, 2.07 and 1.65 at fillings $7/19 \approx 1/3$, 1 and $30/19 \approx 3/2$ respectively. For rhombohedral lattice, r_s is slightly lower due to larger total area, with values 2.6 at half-filling and 2.13 at $3/2$ filling. Although r_s value for $1/3$ filling is smaller by an order of magnitude that is needed for 2DEG Wigner crystallization ($r_s \approx 30 - 35$ ⁴⁵), the crystallization occurs as excited state, indicating a transition to Wigner crystal phase. This effect is due to the moiré potential with large V_m (25 meV) which is not taken into account in terms of band effective mass in the calculation of r_s given by equation 1.12. For $V_m = 6.3$ meV, the electrons have considerably larger kinetic energies, therefore crystallization does not happen even though r_s values are of similar order of magnitude to that for $1/3$ -filling.

To summarize, finite moiré potential is designed and implemented into CHAMP⁴⁶ to perform VMC and DMC simulations of finite MoSe₂/WS₂ heterostructures. A python code to determine MFH ground state orbitals is developed to be used along with TB orbitals as Slater determinants in VMC and DMC calculations. Itinerant ferromagnetism is observed for finite lattices near $\nu = 3/2$ where van Hove singularity occurs. Wigner crystal phase emerges as excited state for $\nu \approx 1/3$ larger moiré potential amplitude. For future work, we consider increasing the lattice size to explore itinerant ferromagnetism further between $\nu = 1$ and $\nu = 3/2$, specifically for $\nu \gtrsim 1$, as shown in Figure 1.5b by the experimental study of Ciorciaro et. al.³² Increasing system size also could also allow us to probe ferrimagnetic behavior for $\nu > 3/2$ in more detail.

REFERENCES

1. Novoselov, K. S.; Geim, A. K.; Morozov, S. V.; Jiang, D.; Zhang, Y.; Dubonos, S. V.; Grigorieva, I. V.; Firsov, A. A. Electric Field Effect in Atomically Thin Carbon Films. *Science* **2004**, *306*, 666–669.
2. Manzeli, S.; Ovchinnikov, D.; Pasquier, D.; Yazyev, O. V.; Kis, A. 2D transition metal dichalcogenides. *Nature Reviews Materials* **2017**, *2*, 17033.
3. Nakada, K.; Fujita, M.; Dresselhaus, G.; Dresselhaus, M. S. Edge state in graphene ribbons: Nanometer size effect and edge shape dependence. *Physical Review B* **1996**, *54*, 17954–17961.
4. Gunst, T.; Markussen, T.; Jauho, A.-P.; Brandbyge, M. Thermoelectric properties of finite graphene antidot lattices. *Physical Review B* **2011**, *84*, 155449.
5. McCann, E. Asymmetry gap in the electronic band structure of bilayer graphene. *Physical Review B* **2006**, *74*, 161403.
6. Zhang, C.; Gong, C.; Nie, Y.; Min, K.-A.; Liang, C.; Oh, Y. J.; Zhang, H.; Wang, W.; Hong, S.; Colombo, L.; Wallace, R. M.; Cho, K. Systematic study of electronic structure and band alignment of monolayer transition metal dichalcogenides in Van der Waals heterostructures. *2D Materials* **2016**, *4*, 015026.
7. Mott, N. F. Metal-Insulator Transition. *Reviews of Modern Physics* **1968**, *40*, 677–683.
8. Imada, M.; Fujimori, A.; Tokura, Y. Metal-insulator transitions. *Reviews of Modern Physics* **1998**, *70*, 1039–1263.
9. Wigner, E. On the Interaction of Electrons in Metals. *Physical Review* **1934**, *46*, 1002–1011.
10. Xu, Y.; Liu, S.; Rhodes, D. A.; Watanabe, K.; Taniguchi, T.; Hone, J.; Elser, V.; Mak, K. F.; Shan, J. Correlated insulating states at fractional fillings of moiré superlattices. *Nature* **2020**, *587*, 214–218.

11. Regan, E. C.; Wang, D.; Jin, C.; Bakti Utama, M. I.; Gao, B.; Wei, X.; Zhao, S.; Zhao, W.; Zhang, Z.; Yumigeta, K.; Blei, M.; Carlström, J. D.; Watanabe, K.; Taniguchi, T.; Tongay, S.; Crommie, M.; Zettl, A.; Wang, F. Mott and generalized Wigner crystal states in WSe₂/WS₂ moiré superlattices. *Nature* **2020**, *579*, 359–363.
12. Huang, X.; Wang, T.; Miao, S.; Wang, C.; Li, Z.; Lian, Z.; Taniguchi, T.; Watanabe, K.; Okamoto, S.; Xiao, D.; Shi, S.-F.; Cui, Y.-T. Correlated insulating states at fractional fillings of the WS₂/WSe₂ moiré lattice. *Nature Physics* **2021**, *17*, 715–719.
13. Zhou, C.; Newns, D. M.; Misewich, J. A.; Pattnaik, P. C. A field effect transistor based on the Mott transition in a molecular layer. *Applied Physics Letters* **1997**, *70*, 598–600.
14. Newns, D. M.; Misewich, J. A.; Tsuei, C. C.; Gupta, A.; Scott, B. A.; Schrott, A. Mott transition field effect transistor. *Applied Physics Letters* **1998**, *73*, 780–782.
15. Yamamoto, H. M. Phase-Transition Devices Based on Organic Mott Insulators. *Bulletin of the Chemical Society of Japan* **2021**, *94*, 2505–2539.
16. Cao, Y.; Fatemi, V.; Fang, S.; Watanabe, K.; Taniguchi, T.; Kaxiras, E.; Jarillo-Herrero, P. Unconventional superconductivity in magic-angle graphene superlattices. *Nature* **2018**, *556*, 43–50.
17. Marković, D.; Mizrahi, A.; Querlioz, D.; Grollier, J. Physics for neuromorphic computing. *Nature Reviews Physics* **2020**, *2*, 499–510.
18. Bistritzer, R.; MacDonald, A. H. Moiré; bands in twisted double-layer graphene. *Proceedings of the National Academy of Sciences* **2011**, *108*, 12233–12237.
19. Kim, K.; DaSilva, A.; Huang, S.; Fallahazad, B.; Larentis, S.; Taniguchi, T.; Watanabe, K.; LeRoy, B. J.; MacDonald, A. H.; Tutuc, E. Tunable moiré; bands and strong correlations in small-twist-angle bilayer graphene. *Proceedings of the National Academy of Sciences* **2017**, *114*, 3364–3369.
20. Cao, Y.; Fatemi, V.; Demir, A.; Fang, S.; Tomarken, S. L.; Luo, J. Y.; Sanchez-Yamagishi, J. D.; Watanabe, K.; Taniguchi, T.; Kaxiras, E.; Ashoori, R. C.; Jarillo-Herrero, P. Correlated insulator behaviour at half-filling in magic-angle graphene superlattices. *Nature* **2018**, *556*, 80–84.

21. Xiao, D.; Liu, G.-B.; Feng, W.; Xu, X.; Yao, W. Coupled Spin and Valley Physics in Monolayers of MoS₂ and Other Group-VI Dichalcogenides. *Physical Review Letters* **2012**, *108*, 196802.
22. Wu, F.; Lovorn, T.; Tutuc, E.; MacDonald, A. H. Hubbard Model Physics in Transition Metal Dichalcogenide Moiré Bands. *Physical Review Letters* **2018**, *121*, 026402.
23. Jin, C.; Regan, E. C.; Yan, A.; Iqbal Bakti Utama, M.; Wang, D.; Zhao, S.; Qin, Y.; Yang, S.; Zheng, Z.; Shi, S.; Watanabe, K.; Taniguchi, T.; Tongay, S.; Zettl, A.; Wang, F. Observation of moiré excitons in WSe₂/WS₂ heterostructure superlattices. *Nature* **2019**, *567*, 76–80.
24. Zhang, Y.; Yuan, N. F. Q.; Fu, L. Moiré quantum chemistry: Charge transfer in transition metal dichalcogenide superlattices. *Physical Review B* **2020**, *102*, 201115.
25. Tang, Y.; Li, L.; Li, T.; Xu, Y.; Liu, S.; Barmak, K.; Watanabe, K.; Taniguchi, T.; MacDonald, A. H.; Shan, J.; Mak, K. F. Simulation of Hubbard model physics in WSe₂/WS₂ moiré superlattices. *Nature* **2020**, *579*, 353–358.
26. Tang, Y.; Gu, J.; Liu, S.; Watanabe, K.; Taniguchi, T.; Hone, J.; Mak, K. F.; Shan, J. Tuning layer-hybridized moiré excitons by the quantum-confined Stark effect. *Nature Nanotechnology* **2021**, *16*, 52–57.
27. Chiu, M.-H.; Zhang, C.; Shiu, H.-W.; Chuu, C.-P.; Chen, C.-H.; Chang, C.-Y. S.; Chen, C.-H.; Chou, M.-Y.; Shih, C.-K.; Li, L.-J. Determination of band alignment in the single-layer MoS₂/WSe₂ heterojunction. *Nature Communications* **2015**, *6*, 7666.
28. Kistner-Morris, J.; Shi, A.; Liu, E.; Arp, T.; Farahmand, F.; Taniguchi, T.; Watanabe, K.; Aji, V.; Lui, C. H.; Gabor, N. Electric-field tunable Type-I to Type-II band alignment transition in MoSe₂/WS₂ heterobilayers. *Nature Communications* **2024**, *15*, 4075.
29. Hu, N. C.; MacDonald, A. H. Competing magnetic states in transition metal dichalcogenide moiré materials. *Physical Review B* **2021**, *104*, 214403.
30. Morales-Durán, N.; MacDonald, A. H.; Potasz, P. Metal-insulator transition in transition metal dichalcogenide heterobilayer moiré superlattices. *Physical Review B* **2021**, *103*, L241110.
31. Morales-Durán, N.; Potasz, P.; MacDonald, A. H. Magnetism and quantum melting in moiré-material Wigner crystals. *Physical Review B* **2023**, *107*, 235131.

32. Ciorciaro, L.; Smoleński, T.; Morera, I.; Kiper, N.; Hiestand, S.; Kroner, M.; Zhang, Y.; Watanabe, K.; Taniguchi, T.; Demler, E.; İmamoğlu, A. Kinetic magnetism in triangular moiré materials. *Nature* **2023**, *623*, 509–513.
33. Potasz, P.; Morales-Durán, N.; Hu, N. C.; MacDonald, A. H. Itinerant ferromagnetism in transition metal dichalcogenide moiré superlattices. *Physical Review B* **2024**, *109*, 045144.
34. Wu, F.; Lovorn, T.; MacDonald, A. H. Topological Exciton Bands in Moiré Heterojunctions. *Physical Review Letters* **2017**, *118*, 147401.
35. Zhang, C.; Chuu, C.-P.; Ren, X.; Li, M.-Y.; Li, L.-J.; Jin, C.; Chou, M.-Y.; Shih, C.-K. Interlayer couplings, Moiré patterns, and 2D electronic superlattices in MoS₂ / WSe₂ hetero-bilayers. *Science Advances* **2017**, *3*, e1601459.
36. Li, S.; Zheng, H.; Ding, J.; Wu, B.; He, J.; Liu, Z.; Liu, Y. Dynamic control of moiré potential in twisted WS₂—WSe₂ heterostructures. *Nano Research* **2022**, *15*, 7688–7694.
37. Tang, Y.; Su, K.; Li, L.; Xu, Y.; Liu, S.; Watanabe, K.; Taniguchi, T.; Hone, J.; Jian, C.-M.; Xu, C.; Mak, K. F.; Shan, J. Evidence of frustrated magnetic interactions in a Wigner–Mott insulator. *Nature Nanotechnology* **2023**, *18*, 233–237.
38. Morales-Durán, N.; Hu, N. C.; Potasz, P.; MacDonald, A. H. Nonlocal Interactions in Moiré Hubbard Systems. *Physical Review Letters* **2022**, *128*, 217202.
39. Sakurai, J. J.; Napolitano, J., *Modern Quantum Mechanics*, 2nd ed.; Cambridge University Press: Cambridge, England, 2017.
40. Santiago, J. M.; Huang, C.-L.; Morosan, E. Itinerant magnetic metals. *Journal of Physics: Condensed Matter* **2017**, *29*, 373002.
41. Hanisch, T.; Kleine, B.; Ritzl, A.; Müller-Hartmann, E. Ferromagnetism in the Hubbard model: instability of the Nagaoka state on the triangular, honeycomb and kagome lattices. *Annalen der Physik* **1995**, *507*, 303–328.
42. Simon, S. H., *The Oxford Solid State Basics*; Oxford University Press: London, England, 2013.
43. Giuliani, G.; Vignale, G., *Quantum Theory of the Electron Liquid*; Cambridge University Press: Cambridge, England, 2005.

44. Güçlü, A. D.; Potasz, P.; Korkusinski, M.; Hawrylak, P. In *Graphene Quantum Dots; Nanoscience and technology*; Springer Berlin Heidelberg: Berlin, Heidelberg, 2014.
45. Ghosal, A.; Güçlü, A. D.; Umrigar, C. J.; Ullmo, D.; Baranger, H. U. Incipient Wigner localization in circular quantum dots. *Physical Review B* **2007**, *76*, 085341.
46. Umrigar, C. J.; C., F.; Toulouse, J.; Güçlü, A. D. Cornell-Holland Ab-initio Materials Package (CHAMP), extended to 2D systems.
47. Virtanen, P.; Gommers, R.; Oliphant, T. E.; Haberland, M.; Reddy, T.; Cournapeau, D.; Burovski, E.; Peterson, P.; Weckesser, W.; Bright, J.; van der Walt, S. J.; Brett, M.; Wilson, J.; Millman, K. J.; Mayorov, N.; Nelson, A. R. J.; Jones, E.; Kern, R.; Larson, E.; Carey, C. J.; Polat, İ.; Feng, Y.; Moore, E. W.; VanderPlas, J.; Laxalde, D.; Perktold, J.; Cimrman, R.; Henriksen, I.; Quintero, E. A.; Harris, C. R.; Archibald, A. M.; Ribeiro, A. H.; Pedregosa, F.; van Mulbregt, P.; SciPy 1.0 Contributors SciPy 1.0: Fundamental Algorithms for Scientific Computing in Python. *Nature Methods* **2020**, *17*, 261–272.
48. Harris, C. R.; Millman, K. J.; van der Walt, S. J.; Gommers, R.; Virtanen, P.; Cournapeau, D.; Wieser, E.; Taylor, J.; Berg, S.; Smith, N. J.; Kern, R.; Picus, M.; Hoyer, S.; van Kerkwijk, M. H.; Brett, M.; Haldane, A.; del Río, J. F.; Wiebe, M.; Peterson, P.; Gérard-Marchant, P.; Sheppard, K.; Reddy, T.; Weckesser, W.; Abbasi, H.; Gohlke, C.; Oliphant, T. E. Array programming with NumPy. *Nature* **2020**, *585*, 357–362.
49. Hunter, J. D. Matplotlib: A 2D graphics environment. *Computing in Science & Engineering* **2007**, *9*, 90–95.
50. Li, T.; Jiang, S.; Li, L.; Zhang, Y.; Kang, K.; Zhu, J.; Watanabe, K.; Taniguchi, T.; Chowdhury, D.; Fu, L.; Shan, J.; Mak, K. F. Continuous Mott transition in semiconductor moiré superlattices. *Nature* **2021**, *597*, 350–354.
51. Marder, M. P., *Condensed Matter Physics*, 2nd ed.; Wiley-Blackwell: Hoboken, NJ, 2010.
52. Xu, S.; Ezzi, M. M. A.; Balakrishnan, N.; Garcia-Ruiz, A.; Tsim, B.; Mullan, C.; Barrier, J.; Xin, N.; Piot, B. A.; Taniguchi, T.; Watanabe, K.; Carvalho, A.; Mishchenko, A.; Geim, A. K.; Fal’ko, V. I.; Adam, S.; Neto, A. H. C.; Novoselov, K. S.; Shi, Y. Tunable van Hove singularities and correlated states in twisted monolayer–bilayer graphene. *Nature Physics* **2021**, *17*, 619–626.

53. Regan, E. C.; Wang, D.; Paik, E. Y.; Zeng, Y.; Zhang, L.; Zhu, J.; MacDonald, A. H.; Deng, H.; Wang, F. Emerging exciton physics in transition metal dichalcogenide heterobilayers. *Nature Reviews Materials* **2022**, *7*, 778–795.
54. Castro Neto, A. H.; Guinea, F.; Peres, N. M. R.; Novoselov, K. S.; Geim, A. K. The electronic properties of graphene. *Reviews of Modern Physics* **2009**, *81*, 109–162.
55. Martin, R. M., *Electronic structure*; Cambridge University Press: Cambridge, England, 2004.
56. Mahan, G. D., *Many-particle physics*, 3rd ed.; Physics of Solids and Liquids; Kluwer Academic/Plenum: New York, NY, 2000.
57. Altıntaş, A. Electronic, magnetic and optical properties of disordered graphene quantum dots, Ph.D. Thesis, Izmir Institute of Technology, 2018.
58. Foulkes, W. M. C.; Mitas, L.; Needs, R. J.; Rajagopal, G. Quantum Monte Carlo simulations of solids. *Reviews of Modern Physics* **2001**, *73*, 33–83.
59. Toulouse, J.; Assaraf, R.; Umrigar, C. J. In *Electron Correlation in Molecules – ab initio Beyond Gaussian Quantum Chemistry*, Hoggan, P. E., Ozdogan, T., Eds.; Advances in Quantum Chemistry, Vol. 73; Academic Press: 2016, pp 285–314.
60. Güçlü, A. D.; Jeon, G. S.; Umrigar, C. J.; Jain, J. K. Quantum Monte Carlo study of composite fermions in quantum dots: The effect of Landau-level mixing. *Physical Review B* **2005**, *72*, 205327.
61. Yang, Y.; Morales, M. A.; Zhang, S. Metal-Insulator Transition in a Semiconductor Heterobilayer Model. *Physical Review Letters* **2024**, *132*, 076503.
62. Bedanov, V. M.; Peeters, F. M. Ordering and phase transitions of charged particles in a classical finite two-dimensional system. *Physical Review B* **1994**, *49*, 2667–2676.

VITA

Mustafa Neşet ÇINAR

Education

- **2018-2024** Ph.D. in Department of Materials Science and Engineering
Izmir Institute of Technology
- **2015-2018** M.Sc. in Department of Materials Science and Engineering
Izmir Institute of Technology
- **2011-2015** B.Sc. in Department of Physics
Izmir Institute of Technology

Employment

- **2020-Present** Research and Teaching Assistant at Izmir Institute of Technology
Courses Assisted
 - MSE 120 - Introduction to Computer Programming
 - MSE 215 - Materials Physics
 - MSE 222 - Applied Mathematics for MSE
 - MSE 305 - Transport Phenomena
 - MSE 312 - Numerical Methods and Modeling

Participation in Funded Research Activities

- Scholarship student - TÜBİTAK Project No. 115F445
- Scholarship student - TÜBİTAK Project No. 117F480
- Scholarship student - TÜBİTAK Project No. 122F345

Publications

- Çınar, M. N., Antidormi, A., Nguyen, V., Kovtun, A., Lara-Avila, S., Liscio, A., Charlier, J., Roche, S., and Sevinçli, H. (2022). Toward optimized charge transport in multilayer reduced graphene oxides. *Nano Letters*, 22(6), 2202–2208.
- Çınar, M. N., Sargın, G. Ö., Sevim, K., Özdamar, B., Kurt, G., and Sevinçli, H. (2021). Ballistic thermoelectric transport properties of two-dimensional group III-VI monolayers. *Physical Review. B/Physical Review. B*, 103(16).
- Çınar, M. N., and Sevinçli, H. (2020). Dimensional crossover and enhanced thermoelectric efficiency due to broken symmetry in graphene antidot lattices. *Physical Review Applied*, 14(2).
- Özdamar, B., Özbal, G., Çınar, M. N., Sevim, K., Kurt, G., Kaya, B., and Sevinçli, H. (2018). Structural, vibrational, and electronic properties of single-layer hexagonal crystals of group IV and V elements. *Physical Review. B/Physical Review. B*, 98(4).